



LAWRENCE  
LIVERMORE  
NATIONAL  
LABORATORY

LLNL-JRNL-657078

# The effect of shock dynamics on compressibility of ignition-scale NIF implosions

A. B. Zylstra, J. A. Frenje, F. H. Seguin, D. G. Hicks, E. Dewald, H. Robey, J. R. Rygg, N. B. Meezan, M. J. Rosenberg, H. G. Rinderknecht, S. Friedrich, R. Bionta, R. Olson, J. Atherton, M. Barrios, P. Bell, R. Benedetti, L. Berzak Hopkins, R. Betti, D. Bradley, D. Callahan, D. Casey, G. Collins, S. Dixit, T. Doeppner, D. Edgell, M. J. Edwards, M. Gatu Johnson, S. Glenn, S. Glenzer, G. Grim, S. Hatchett, O. Jones, S. Khan, J. Kilkenny, J. Kline, J. Knauer, A. Kritcher, G. Kyrala, O. Landen, S. LePape, C. K. Li, J. Lindl, T. Ma, A. Mackinnon, A. Macphee, M. J. Manuel, D. Meyerhofer, J. Moody, E. Moses, S. Nagel, A. Nikroo, A. Pak, T. Parham, R. D. Petrasso, R. Prasad, J. Ralph, M. Rosen, J. S. Ross, et al.

July 14, 2014

Physics of Plasmas

## **Disclaimer**

---

This document was prepared as an account of work sponsored by an agency of the United States government. Neither the United States government nor Lawrence Livermore National Security, LLC, nor any of their employees makes any warranty, expressed or implied, or assumes any legal liability or responsibility for the accuracy, completeness, or usefulness of any information, apparatus, product, or process disclosed, or represents that its use would not infringe privately owned rights. Reference herein to any specific commercial product, process, or service by trade name, trademark, manufacturer, or otherwise does not necessarily constitute or imply its endorsement, recommendation, or favoring by the United States government or Lawrence Livermore National Security, LLC. The views and opinions of authors expressed herein do not necessarily state or reflect those of the United States government or Lawrence Livermore National Security, LLC, and shall not be used for advertising or product endorsement purposes.

# The effect of shock dynamics on compressibility of ignition-scale NIF implosions

A. B. Zylstra,<sup>1, a)</sup> J. A. Frenje,<sup>1</sup> F. H. Séguin,<sup>1</sup> D. G. Hicks,<sup>2</sup> E. Dewald,<sup>2</sup> H. Robey,<sup>2</sup> J. R. Rygg,<sup>2</sup> N. B. Meezan,<sup>2</sup> M. J. Rosenberg,<sup>1</sup> H. G. Rinderknecht,<sup>1</sup> S. Friedrich,<sup>2</sup> R. Bionta,<sup>2</sup> R. Olson,<sup>3,4</sup> J. Atherton,<sup>2</sup> M. Barrios,<sup>2</sup> P. Bell,<sup>2</sup> R. Benedetti,<sup>2</sup> L. Berzak Hopkins,<sup>2</sup> R. Betti,<sup>5</sup> D. Bradley,<sup>2</sup> D. Callahan,<sup>2</sup> D. Casey,<sup>2</sup> G. Collins,<sup>2</sup> S. Dixit,<sup>2</sup> T. Döppner,<sup>2</sup> D. Edgell,<sup>5</sup> M. J. Edwards,<sup>2</sup> M. Gatu Johnson,<sup>1</sup> S. Glenn,<sup>2</sup> S. Glenzer,<sup>2</sup> G. Grim,<sup>4</sup> S. Hatchett,<sup>2</sup> O. Jones,<sup>2</sup> S. Khan,<sup>2</sup> J. Kilkeny,<sup>6</sup> J. Kline,<sup>4</sup> J. Knauer,<sup>5</sup> A. Kritcher,<sup>2</sup> G. Kyrala,<sup>4</sup> O. Landen,<sup>2</sup> S. LePape,<sup>2</sup> C. K. Li,<sup>1</sup> J. Lindl,<sup>2</sup> T. Ma,<sup>2</sup> A. Mackinnon,<sup>2</sup> A. Macphée,<sup>2</sup> M. J.-E. Manuel,<sup>1</sup> D. Meyerhofer,<sup>5</sup> J. Moody,<sup>2</sup> E. Moses,<sup>2</sup> S. Nagel,<sup>2</sup> A. Nikroo,<sup>6</sup> A. Pak,<sup>2</sup> T. Parham,<sup>2</sup> R. D. Petrasso,<sup>1</sup> R. Prasad,<sup>2</sup> J. Ralph,<sup>2</sup> M. Rosen,<sup>2</sup> J. S. Ross,<sup>2</sup> T. C. Sangster,<sup>5</sup> S. Sepke,<sup>2</sup> N. Sinenian,<sup>1</sup> H. W. Sio,<sup>1</sup> B. Spears,<sup>2</sup> P. Springer,<sup>2</sup> R. Tommasini,<sup>2</sup> R. Town,<sup>2</sup> S. Weber,<sup>2</sup> D. Wilson,<sup>4</sup> R. Zacharias,<sup>2</sup> and ...<sup>2</sup>

<sup>1)</sup> *Plasma Science and Fusion Center, Massachusetts Institute of Technology, Cambridge, MA 02139, USA*

<sup>2)</sup> *Lawrence Livermore National Laboratory, Livermore, CA 94550, USA*

<sup>3)</sup> *Sandia National Laboratory, Albuquerque, NM 87185, USA*

<sup>4)</sup> *Los Alamos National Laboratory, Los Alamos, NM 87545, USA*

<sup>5)</sup> *Laboratory for Laser Energetics, University of Rochester, Rochester, NY 14623, USA*

<sup>6)</sup> *General Atomics, San Diego, CA 92186, USA*

(Dated: 9 July 2014)

The effects of shock dynamics on compressibility of indirect-drive ignition-scale surrogate implosions, CH shells filled with D<sup>3</sup>He gas, have been studied using charged-particle spectroscopy. Spectral measurements of D<sup>3</sup>He protons produced at the shock-bang time probe the shock dynamics and in-flight characteristics of an implosion. The proton shock yield is found to vary by over an order of magnitude. A simple model relates the observed yield to incipient hot-spot adiabat, suggesting that implosions with rapid radiation-power increase during the main drive pulse may have a 2× higher hot-spot adiabat, potentially reducing compressibility. A self-consistent 1-D implosion model was used to infer the areal density ( $\rho R$ ) and the shell center-of-mass radius ( $R_{cm}$ ) from the downshift of the shock-produced D<sup>3</sup>He protons. The observed  $\rho R$  at shock-bang time is substantially higher for implosions where the laser drive is on until near the compression bang time (‘short-coast’), while longer-coasting implosions have lower  $\rho R$ . This corresponds to a much larger temporal difference between the shock- and compression-bang time in the long-coast implosions ( $\sim 800$ ps) than in the short-coast ( $\sim 400$ ps); this will be verified with a future direct bang-time diagnostic. This model-inferred differential bang time contradicts radiation-hydrodynamic simulations, which predict constant 700 – 800ps differential independent of coasting time; this result is potentially explained by uncertainties in modeling late-time ablation drive on the capsule. In an ignition experiment, an earlier shock-bang time resulting in an earlier onset of shell deceleration, potentially reducing compression and thus fuel  $\rho R$ .

PACS numbers: 52.57.-z, 52.35.Tc, 52.70.Nc

## I. INTRODUCTION

In the inertial confinement approach to laboratory fusion,<sup>1,2</sup> substantial compression of the fuel is required in MJ-scale implosions such as those at the National Ignition Facility (NIF)<sup>3</sup>. A spherical convergence ratio (ratio of initial to final radius) of  $\sim 35$  is necessary to achieve the conditions required for ignition and energy gain.<sup>2</sup>

While ignition experiments at the NIF use targets with cryogenic layers of DT fuel, numerous surrogate implosions have been conducted where the layer of DT

ice is replaced with a surrogate mass of ablator material (CH). The hydrodynamics before deceleration are nearly identical for the cryogenic layered and surrogate implosions,<sup>4</sup> enabling complementary studies and diagnostics of implosion dynamics, such as symmetry<sup>5,6</sup> and velocity.<sup>7,8</sup> One of the main objectives of using these surrogate implosions is to characterize the implosion at various stages to benchmark radiation-hydrodynamics simulations.<sup>4,9–11</sup>

In an implosion, a series of spherically converging shocks are launched with increasing strength. These shocks eventually coalesce at the capsule’s inner edge and then converge at the center of the implosion. The final shock ‘rebounds’ and briefly creates high-ion-temperature conditions at the center of the implosion.

<sup>a)</sup> Electronic mail: zylstra@mit.edu

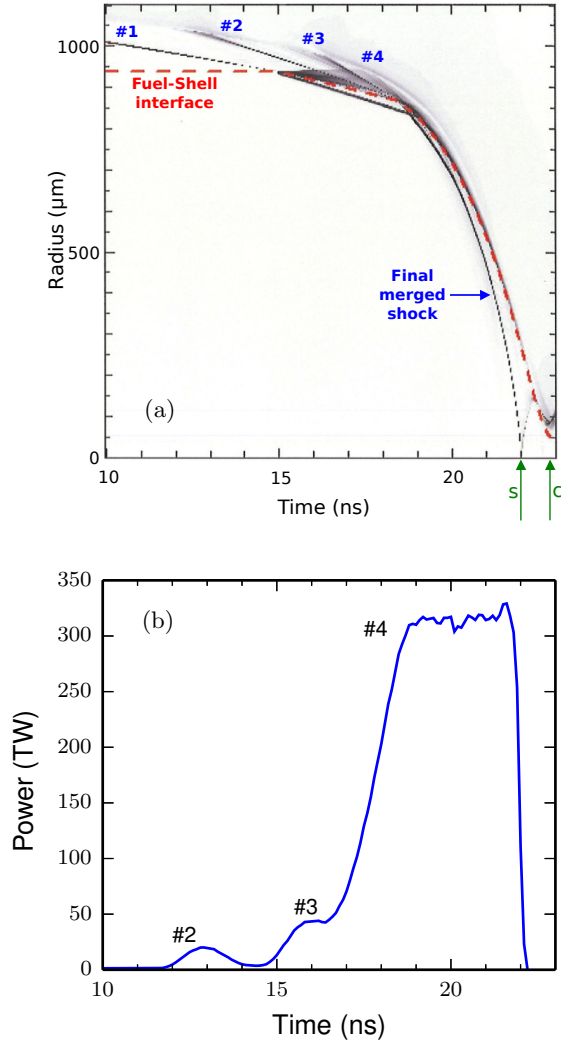


FIG. 1: NIF surrogate shot N120408-001-999 (CH shell with  $D^3He$  gas, see Fig. 3). **(a)** Simulated shock trajectory, visualized as the pressure gradient  $|(1/P)dP/dr|$  where black indicates a higher value. The shock plot shows the four shocks launched into the shell, which merge to form the final shock that travels to the center where it rebounds, increasing the temperature and density, creating the shock burn at 22.03 ns. The compression bang time is at 22.83ns. Simulated shock (s) and compression (c) bang times are indicated by the arrows. **(b)** Laser pulse (foot before 10 ns not shown). In the drive, the pickets at  $\sim 13$  and  $\sim 16$  ns launch the 2<sup>nd</sup> and 3<sup>rd</sup> shocks respectively, with the 4<sup>th</sup> launched by the rise to peak power.

In the case of surrogate implosions at NIF with a  $D^3He$  gas fill, this ion temperature is high enough to produce energetic protons via the fusion reaction:



For surrogate implosions at the NIF, this ‘shock burn’ occurs several hundred ps before the main compression

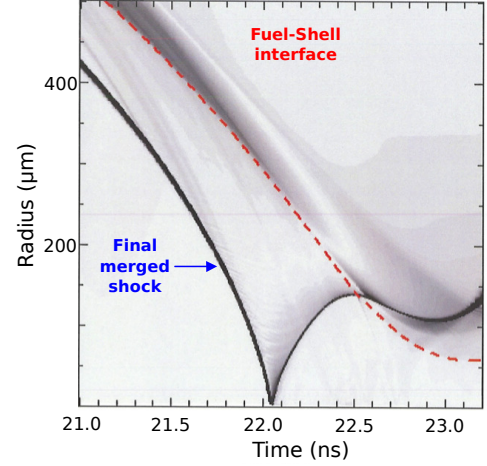


FIG. 2: Shock trajectory through rebound, shock burn, and compression phases, for the same simulation as Fig. 1a.

burn, and is approximately concurrent with peak shell implosion velocity. This is shown for a typical surrogate implosion in Fig. 1 using the radiation-hydrodynamics code HYDRA<sup>11</sup>, where the simulated shock trajectories for the four launched shocks and final merged shock are shown in Fig. 1a as contours of the normalized pressure gradient  $|(1/P)dP/dr|$ . The laser pulse is shown in Fig. 1b, a detailed view of the shock dynamics around the shock-bang time and compression-bang time is shown in Fig. 2, and the capsule dimensions are shown in Fig. 3.

After the final merged shock rebounds at  $\sim 22$  ns the shock burn occurs over  $\sim 100$  ps, producing energetic  $D^3He$  protons (Eq. 1). These escaping protons are used to probe the in-flight characteristics of the shell at a radius of  $\sim 250\mu m$ .

$D^3He$  proton spectroscopy is a well-developed technique for diagnosing inertial fusion implosions<sup>12–16</sup> at the OMEGA laser facility<sup>17</sup> and now at the NIF.<sup>18,19</sup> A typical measured  $D^3He$  proton spectrum is shown in Fig. 4. The protons have been energy downshifted to  $\sim 11.5$  MeV from the birth energy of 14.7 MeV. The downshift is

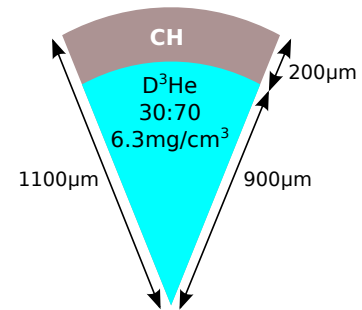


FIG. 3: Typical NIF surrogate capsule (see Table II for more information).

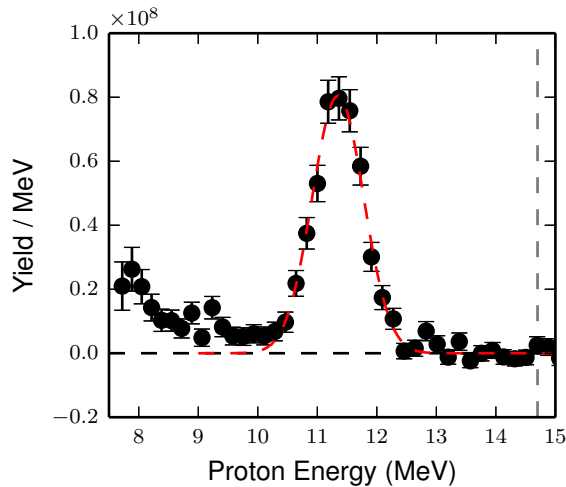


FIG. 4: Sample  $D^3He$  proton spectrum from NIF shot N101004-002-999, measured on the equator (DIM 90-78

Wedge Range Filter (WRF) #1) after hohlraum correction. The  $D^3He$  average birth energy of 14.7 MeV is shown by the vertical dashed line. The red dashed line is a Gaussian fit to the spectrum. Surplus protons at low energy,  $\sim 8 - 9$  MeV, are due to the onset of compression burn. More details are given in Appendix A

caused by Coulomb collisions with the imploding plasma electrons<sup>20</sup>, and the observed downshift can be related to the implosion areal density ( $\rho R$ ) using a charged-particle stopping theory<sup>21</sup>. The shock yield observed ( $8.7 \times 10^7$ ) is related to the final merged shock strength<sup>16,22</sup>. The center-of-mass radius ( $R_{cm}$ ) of the imploding shell is inferred in addition to  $\rho R$  using 1-D modeling discussed in Section II.

As a probe of the implosion shock dynamics, this technique is unique in that it probes the strength of the final merged shock when it hits and rebounds from the center of the implosion. This measurement is complementary to the shock-timing measurements of the shock velocity that use an interferometry technique,<sup>23</sup> which has been highly successful at understanding the shock dynamics in the shell for radii larger than  $600 - 700 \mu m$ .<sup>24-27</sup> At smaller radii the interferometry measurements ‘blank’. As a result, the interferometry measurement would not see any additional shocks launched later in the implosion after the blanking, and does not probe the shock dynamics in the gas, when spherical convergence effects are significant; as the shock strength increases with convergence,<sup>22</sup> non-hydrodynamic behavior may become important.<sup>28,29</sup>

The paper is organized as follows: an implosion model for interpreting the spectral results is presented in Section II. Section III gives an overview of the experiments; Section V discusses a down-selected set of implosions to infer the shock dynamics, Section VI interprets the results and their relevance to implosion compressibility,

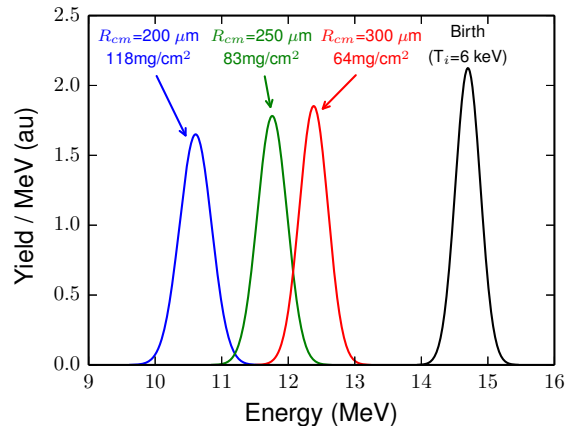


FIG. 5: For illustration, modeled  $D^3He$  proton spectra at birth (black) downshifted through 64 (red), 83 (green), and 118 (blue)  $mg/cm^2$  of  $\rho R$  are shown. The downshifts are calculated with a 1-D self-consistent model. Values of the shell  $R_{cm}$  associated with each spectrum are also shown.

and the paper is concluded in Section VII.

## II. IMPLOSION MODEL

The  $D^3He$  protons slow down monotonically as they traverse any material between the source and spectrometer. The measured proton downshift is directly related to the implosion  $\rho R$  at the time of shock burn. This is illustrated in Fig. 5, which shows the birth spectrum plus modeled spectra for several values of the shell center-of-mass radius ( $R_{cm}$ ) and  $\rho R$  using the model described in this section. These values span the typical range at shock-bang time in NIF implosions.

To relate the measured  $D^3He$  proton spectrum to the implosion conditions, a model involving charged-particle stopping theory<sup>21</sup> is required. The simplest 0-D model is to take a single characteristic plasma composition, density, and electron temperature from a simulation or an estimate, and then use a stopping power theory to calculate  $dE/dr$ . This works well for OMEGA implosions where the dense shell dominates slowing<sup>15</sup>, but for ignition-scale surrogate implosions being conducted at the NIF a significant fraction of proton slowing during the shock burn occurs in the fuel and ablated material. These plasmas have much lower density and higher temperature than the dense shell, so a single choice of plasma conditions cannot accurately describe the entire system.

This necessitates a 1-D self-consistent model, which is constructed using initial target conditions and assumptions about in-flight plasma conditions to specify the density and temperature profiles of the implosion. As the shell converges, the  $\rho R$  increases and the energy of emitted protons decreases. The shell center-of-mass radius

$R_{cm}$  is taken as a free parameter, and thus is varied to obtain  $\rho R(R_{cm})$  with  $\rho R \equiv \int_0^\infty \rho(r) dr$ . Similarly, the energy of protons escaping the implosion is calculated as a function of  $R_{cm}$  by

$$E_p(R_{cm}) = E_0 - \int_0^\infty \frac{dE}{dr}(r, R_{cm}) dr, \quad (2)$$

where  $E_0$  is the average birth energy of the protons. The charged-particle stopping power  $dE/dr$  depends on plasma conditions specified by the model and thus on both  $r$  and  $R_{cm}$ . The Li-Petrasso theory<sup>21</sup> is used in this work.

The initial capsule conditions are used as a model input: the shell material, inner and outer radii, and gas fill (composition and initial pressure). Fig. 3 illustrates the typical capsule dimensions and gas fill. The model makes assumptions about the in-flight characteristics of the implosion, informed by 1-D HYDRA<sup>11</sup> simulations: temperature in the fuel, shell, and ablated mass, the thickness<sup>30</sup> and mass remaining of the shell, and an ablated mass profile.

With the initial conditions and in-flight assumptions, the gas density and  $\rho R$  scale with  $R_{cm}$  as

$$\rho_{\text{gas}} = \rho_{0,\text{gas}} \left( \frac{R_i}{R_{cm} - \Delta R_s/2} \right)^3, \quad (3)$$

$$\rho R_{\text{gas}} = \rho_{\text{gas}} (R_{cm} - \Delta R_s/2), \quad (4)$$

where  $\rho_{0,\text{gas}}$  is the initial gas density,  $R_i$  is the initial inner shell radius, and  $\Delta R_s$  is the in-flight shell thickness.

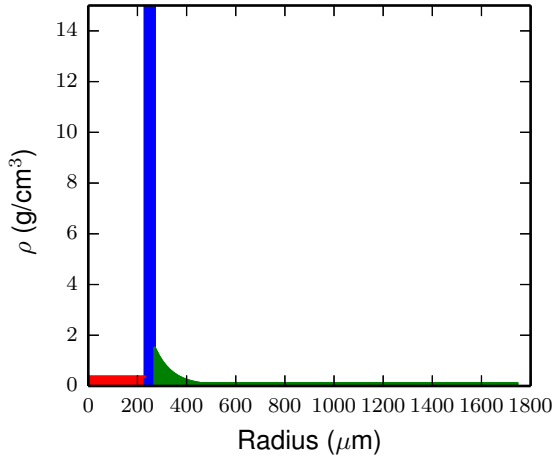


FIG. 6: Density profile used in the 1-D model at  $R_{cm} = 250 \mu\text{m}$ . This center-of-mass shell radius is typical for NIF shots at shock-bang time. The gas material is shown in red ( $8 \text{ mg/cm}^2$ ), the shell is shown in blue ( $53 \text{ mg/cm}^2$ ), and the ablated mass is in green ( $23 \text{ mg/cm}^2$ ).

Similarly, the shell conditions are given by

$$\rho_{\text{shell}} = \frac{M_{\text{rem}} \rho_{0,\text{shell}} (R_o^3 - R_i^3)}{(R_{cm} + \Delta R_s/2)^3 - (R_{cm} - \Delta R_s/2)^3}, \quad (5)$$

$$\rho R_{\text{shell}} = \rho_{\text{shell}} \Delta R_s, \quad (6)$$

where  $\rho_{0,\text{shell}}$  is the initial shell density,  $M_{\text{rem}}$  is the remaining mass fraction, and  $R_o$  and  $R_i$  are respectively the initial outer and inner radii of the shell.

The ablated mass profile is specified by

$$\rho(r) = \begin{cases} \rho_{\text{max}} \times e^{-(r-r_0)/\lambda} & \text{if } r_0 \leq r \leq r_1 \\ \rho_{\text{min}} & \text{if } r_1 \leq r \leq r_2 \end{cases}, \quad (7)$$

where  $r_0 = R_{cm} + \Delta R_s/2$  is the outer radius of the imploding shell,  $\rho_{\text{max}}$  and  $\rho_{\text{min}}$  are the maximum and minimum densities of ablated material, and  $\lambda$  is a characteristic scale length in the ablation region. The radius  $r_1$  is determined by requiring continuity of the ablated mass density profile as described by Eq. 7, and  $r_2$  is determined by conservation of total mass. The values of  $\rho_{\text{max}}$ ,  $\rho_{\text{min}}$ , and  $\lambda$  are model assumptions. The areal

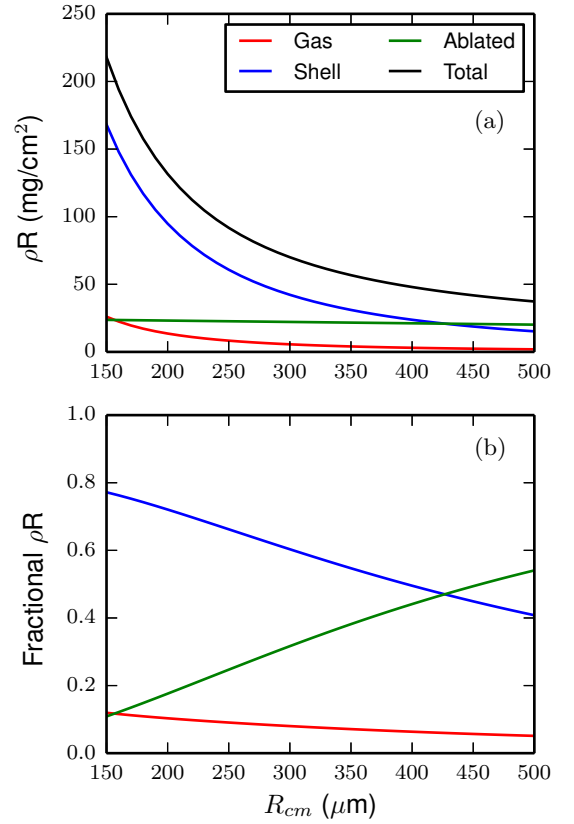


FIG. 7:  $\rho R$  components (gas, shell, and ablated material) as a function of  $R_{cm}$  for typical model parameters. The results are plotted as absolute  $\rho R$  (a), and normalized to the total (b).

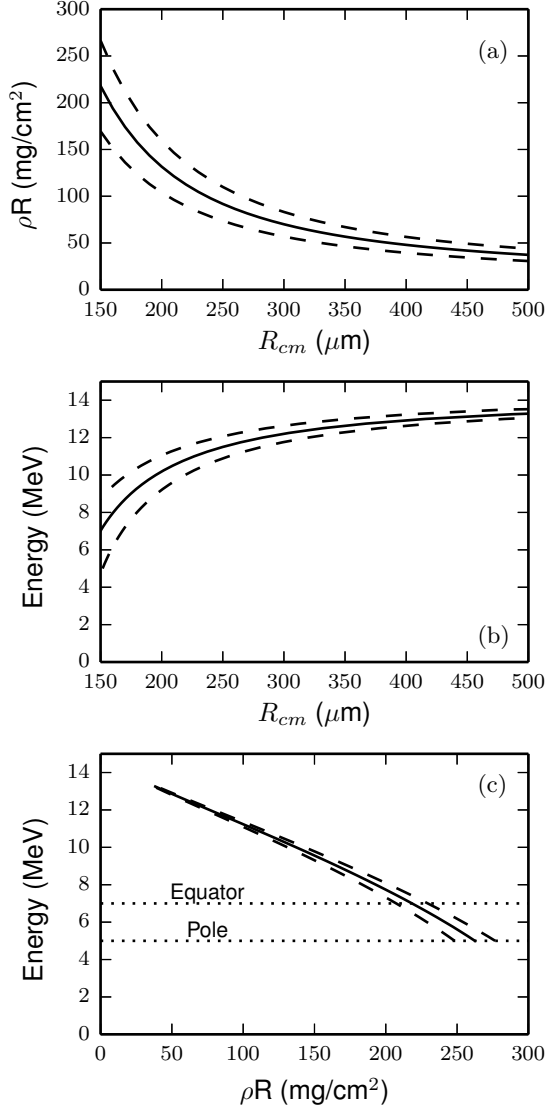


FIG. 8: **(a)** Modeled  $\rho R$  vs  $R_{cm}$ , **(b)** Average energy of emitted protons vs  $R_{cm}$ , and **(c)** Average energy of emitted protons vs  $\rho R$ . The dashed curves indicate the uncertainties in the modeling. The instrumental lower cutoffs are shown in (c) by dotted lines at 5 MeV (pole), and 7 – 8 MeV for the equator, increased due to the energy loss in the hohlraum wall (see Fig. 10).

density of ablated material is

$$\begin{aligned} \rho R_{abl} &= \int_{r_0}^{r_2} \rho(r) dr \\ &= \rho_{\max} \lambda \left[ 1 - e^{-(r_1 - r_0)/\lambda} \right] \\ &\quad + (r_2 - r_1) \rho_{\min}. \end{aligned} \quad (8)$$

An example of the modeled density profile is shown for  $R_{cm} = 250 \mu\text{m}$  in Fig. 6. The components of  $\rho R$ , e.g. Eqs 4, 6, and 8, are calculated as functions of  $R_{cm}$  both in absolute values of  $\text{mg}/\text{cm}^2$  and also as fractions of the

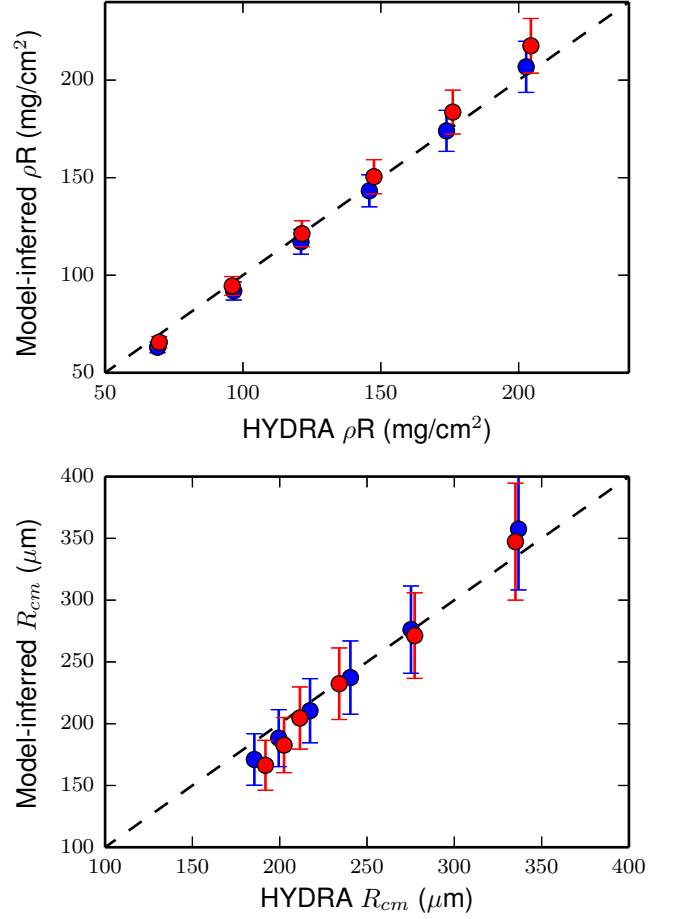


FIG. 9: Comparison between model-inferred  $\rho R$  (top) and  $R_{cm}$  (bottom) using synthetic emitted proton energies from HYDRA simulations, compared to values directly extracted from the simulation. Six time snapshots are used from two simulations: nominal (blue) and high preheat (red).

total  $\rho R$  (Fig. 7). The gas and shell  $\rho R$  depend strongly on convergence (Eqs 4 and 6) while the ablated material  $\rho R$  only increases modestly as  $R_{cm}$  decreases. Thus for  $R_{cm} \sim 200 - 300 \mu\text{m}$ , the shell  $\rho R$  will dominate with 60 – 70% of the total  $\rho R$ .

The final result of the model is the relationships between the three quantities:  $R_{cm}$ ,  $\rho R$ , and emitted proton energy ( $E_p$ ). For the typical parameters, the model produces the curves shown in Fig 8. For completeness we show the  $\rho R$  vs  $R_{cm}$ ,  $E_p$  vs  $R_{cm}$ , and finally the  $\rho R$  vs  $E_p$  curves. Thus the measured quantity ( $E_p$ ) can be converted directly into  $\rho R$  and  $R_{cm}$  using these relationships.

Each quantity used in the model has an associated error bar, which is used to calculate the uncertainty in the inferred quantities. This is done by an in-line sensitivity analysis to variations in the input quantities. For details





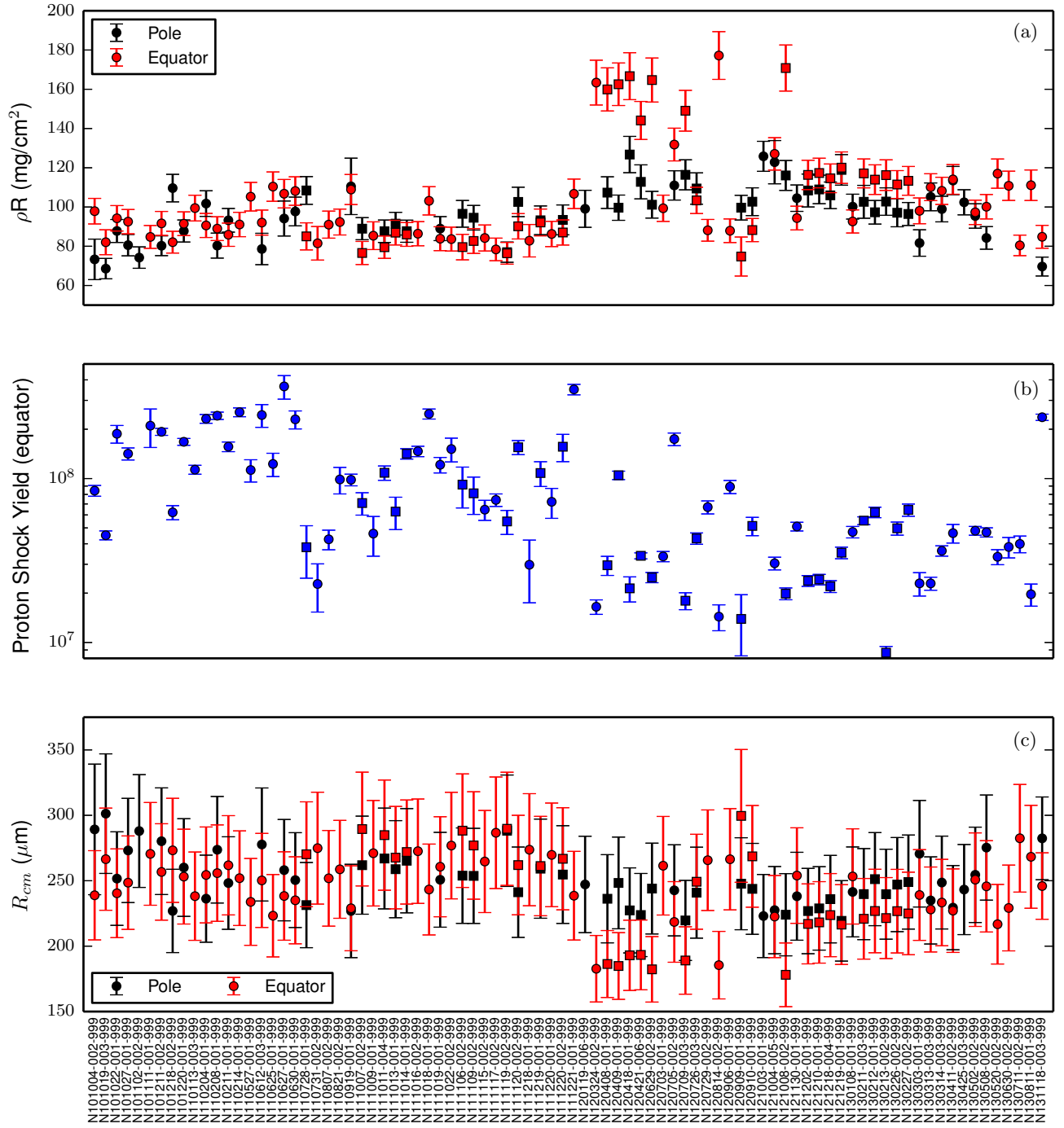


FIG. 11: WRF data for all surrogate implosions. (a) Shock  $\rho R$  data. When available both polar (DIM 0-0) and equatorial data (DIM 90-78) are shown. (b) Shock proton yield measured by WRFs on DIM 90-78. (c) Center-of-mass shell radius ( $R_{cm}$ ) plotted as average values for both pole (DIM 0-0) and equator (DIM 90-78).

#### IV. DATA DOWN-SELECTION

Due to the large shot-to-shot parameter variations during the NIF campaigns, it is necessary to select a subset of implosions with similar overall conditions for detailed analysis. We perform this down-selection using the fol-

lowing criteria:

1. Standard capsules (CH with  $D^3\text{He}$  fill, see Fig. 3)
2. 5.75mm diameter hohlraums
3. WRF data available on both pole and equator

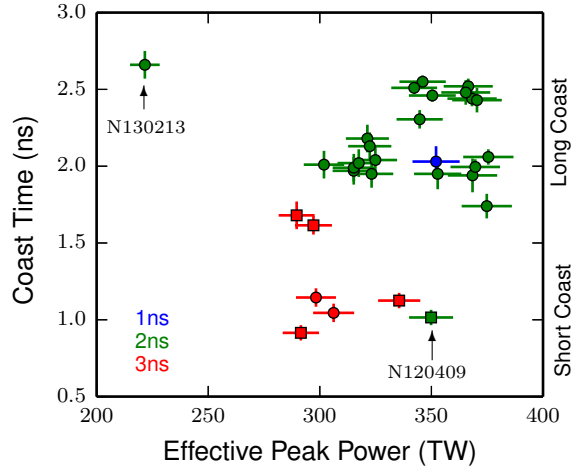


FIG. 12: Coast time and peak power of down-selected experiments. With a few exceptions, implosions have been conducted at low-power, short-coast ( $\sim 300$  TW,  $\sim 1$  ns) conditions or high-power, long-coast ( $\sim 350$  TW,  $\sim 2$  ns) conditions.

#### 4. Low-adiabat ('4-shock') pulse shapes

This reduces the number of shots to 30. Criterion #3 is required to allow for modeling of the observed  $\rho R$  asymmetries (see Fig. 11a and Ref. 19) and determining of average values for  $\rho R$  and  $R_{cm}$ . Shots selected via these criteria are used in subsequent analysis and are denoted in Fig. 11 by square markers.

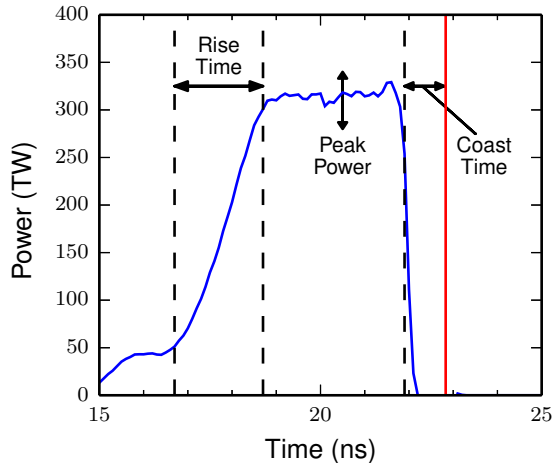


FIG. 13: Relevant variables of the laser pulse: rise time, peak power, and coast time. In this case, the rise time is 2 ns, the peak incident power is 300 TW, and the coasting time is 0.9 ns (short-coast, while long-coast is  $\sim 2$  ns). The bang time is indicated by the red line.

## V. SHOCK DYNAMICS

The shock dynamics of the down-selected set of 30 implosions can now be explored. The observations indicate that the shock dynamics are most sensitive to the peak power of the laser drive, the coasting time of the implosion, and the rise time of the main laser pulse, see Fig. 13.

Since the effective drive experienced by the capsule depends on the absorption of the incident laser light and the effectiveness of conversion to x rays, we add 25 TW to the actual laser power for DU hohlraums to account for the latter, and then multiply by the observed absorption fraction to account for the former. This gives an 'effective peak power' which is used in this work. The coasting time of an implosion is defined as the difference between the end of the laser drive and the measured compression bang time. The rise times used in these experiments are discrete, with design values of 1, 2, or 3 ns.

With these definitions, the main observables (average  $\rho R$  and shock yield) are plotted versus the effective peak power, coasting time, and rise time. The data are shown in Fig. 14. To eliminate the effect of low-mode asymmetries observed in these implosions, this analysis uses an average  $\rho R$  obtained from a fit to the polar and equatorial  $\rho R$  data (see Appendix D and Ref. 19). The different rise times used are differentiated by marker color. Furthermore, the hohlraum material is specified by marker shape: square markers for DU and circular markers for Au hohlraums.

The distribution of implosion parameters used (peak power, coast time, and rise time) is illustrated by Fig. 12. With a few exceptions, the experiments fall into two groups:

1. Low-power ( $\sim 275$ – $325$  TW), short-coast ( $\sim 1$ – $1.5$  ns), slow-rise (3 ns)
2. High-power ( $\sim 325$ – $375$  TW), long-coast ( $\sim 2$ – $2.5$  ns), fast-rise (1 or 2 ns)

Since these two groups are diametrically opposed in all three parameters disentangling their effects requires using a few select implosions that do not fall into these groups. For the rise time a set of three implosions was conducted where only the rise time was varied, significantly aiding this interpretation.

### A. Shock yield interpretation

First, the interpretation of the shock-yield data can be aided by a set of three shots conducted in which only the rise time was varied. This data is shown in Fig. 15a. The faster rise pulse shapes clearly create higher shock yields. This is consistent with the data in Fig. 14f.

Conversely, the coast time (Fig. 14e) has no clear effect on the shock yield, since short- and long- coast times have data with both high- and low- shock yield.

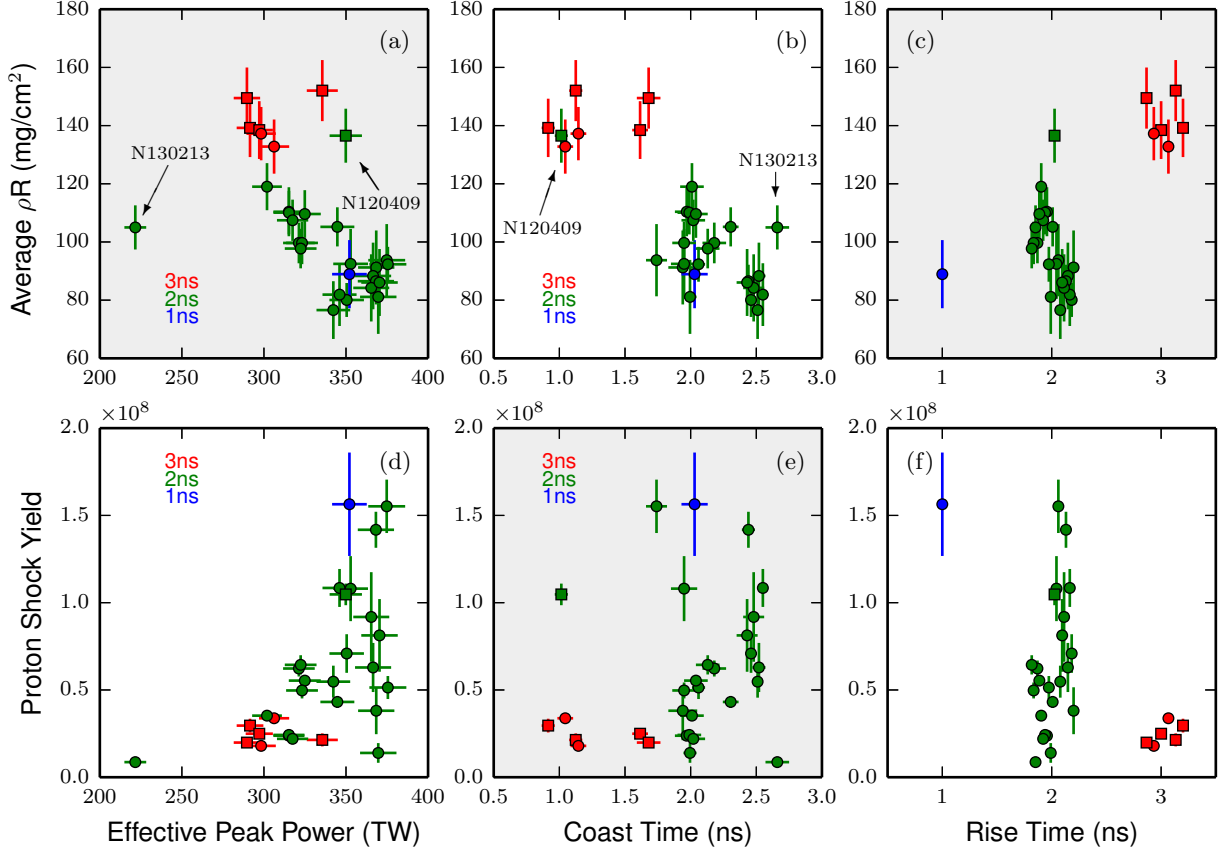


FIG. 14: Shock  $\rho R$  and yield data [ $\rho R$  (a-c) and  $Y_p$  (d-f)] versus effective peak power (a,d), coast time (b,e), and rise time (c,f). For the rise time, points are artificially displaced for clarity around the values 1, 2, or 3 ns (see c,f). Rise time is further specified by point color: 1ns (blue), 2ns (green), and 3ns (red) to improve clarity in the power and coast time plots. Additionally, Au-wall hohlraums are denoted by circular markers, and DU-wall hohlraums by square markers.

For the peak power, the data in Fig. 14d suggests a trend, where lower peak power creates a weaker shock. This is intuitive and consistent with the fact that all low power ( $\lesssim 300$  TW) shots have low yield, but at higher power the shock yield displays significant variation.

We conclude that the faster-rise pulses create shock yields 2 – 3 $\times$  higher (Fig 14f and 15) with other variables constant, and that increasing the peak power may increase the shock yield. We note that the shock yield varies by approximately 15 $\times$  over the dataset, indicating substantial variation in shock strength.

## B. $\rho R$ interpretation

Two shots that do not fit into the overall implosion parameter grouping are essential to understanding the data: N120409, which was a high-power short-coast shot, and N130213 which was a low-power long-coast shot. These two are specifically annotated in Fig. 12 and Fig. 14a-b.

Fig. 14a plots the shock  $\rho R$  versus effective peak

power. Neglecting the results from shots N120409 and N130213, the data show an anti-correlated trend between  $\rho R$  and peak power. However, shots N120409 and N130213 clearly suggest that this trend is due to the preponderance of high-power long-coast and low-power short-coast implosions. For the coasting, a clear trend is observed in Fig. 14b, including both N120409 and N130213 where large coast times generate significantly lower shock  $\rho R$  than short-coast implosions.

In Fig. 15 the set of three shots with a controlled rise time show no change in shock  $\rho R$  as the rise time is varied. This demonstrates that the rise time has no effect on the shock  $\rho R$ ; the apparent trend in Fig. 14c is due to the low coasting times in the 3ns rise implosions.

## C. Estimated shock-bang time

The dependence between shock  $\rho R$  and coast time can be further investigated. Fundamentally, the  $\rho R$  is mainly determined by the shell  $R_{cm}$  at the shock-bang time (see

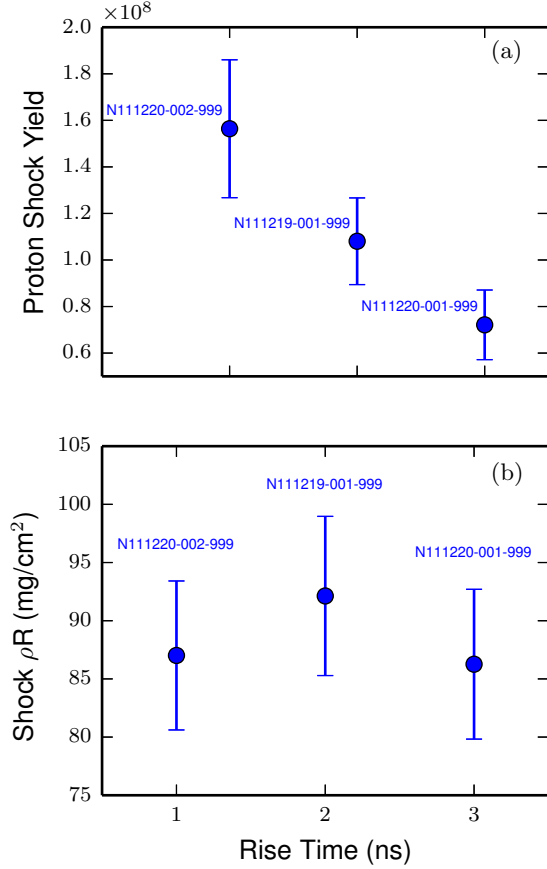


FIG. 15: Shock yield (a) and  $\rho R$  (b) versus rise time for a set of three shots where only the rise time was varied.

Section II).

On many of these shots, simultaneous x-ray radiographs of the implosion trajectory were obtained<sup>7,8,37</sup>, and from the x-ray radiographs,  $R_{cm}(t)$  is determined near the shock-bang time. Presently the shock-bang time is not directly measured, but the combination of the trajectory measurement and WRF-inferred  $R_{cm}$  from shock-produced protons can be used to estimate the shock-bang time. This technique is shown in Fig. 16.

From the x-ray data we know the shell velocity at  $R_{cm} = 200$  or  $300 \mu\text{m}$ . The absolute timing uncertainty of the x-ray measurement relative to compression bang time is  $\pm 50$  ps. We know that the compression-bang time uncertainty is typically  $\pm 50$  ps or better. From this information, combined with the x-ray and proton data, a shock-bang time can be determined relative to compression-bang time:  $\Delta_{BT} \equiv t_{shock} - t_{comp}$ , to remove any variation in absolute implosion timing. The uncertainty in  $R_{cm}$  from this analysis is used to determine the uncertainty in the shock-bang time in addition to the uncertainty in timing of the x-ray measurement and shell velocity.

The shock-bang time is estimated for a set of 14 experiments (a subset of Fig. 14) where x-ray radiography

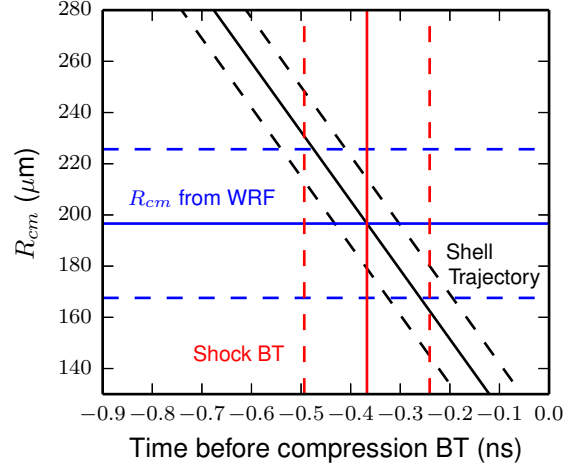


FIG. 16:  $R_{cm}$  versus time before compression-bang time for shot N120408-001-999. As the shell trajectory (black) and  $R_{cm}$  (blue) are determined from x-ray radiography and WRF proton spectroscopy, respectively, the shock-bang time (red) can be estimated. Error bars are shown by dashed lines. For this shot,  $\Delta_{BT} = 0.34 \pm 0.13$  ns.

is available, and shown in Fig. 17. The estimated bang time difference ranges from  $\sim 0.4 - 0.8$  ns. The displayed error bars represent random (shot-to-shot) uncertainties, while the larger systematic uncertainty is  $\pm 0.11$  ns.

For this data, a clear trend is shown where the long-coast implosions have substantially larger differential bang time (more negative  $\Delta_{BT}$ ) than the short-coast shots.

Simulations of  $\Delta_{BT}$  exist for five of these shots (one of which, N120408-001-999, was simulated and presented earlier in Figs. 1 and 2); these simulations are also shown in Fig. 17. The simulations predict a nearly constant  $\Delta_{BT}$  of  $\sim -(0.7 - 0.8)$  ns while the data show a clear trend where long-coast implosions have a larger differential bang time.

## VI. INTERPRETATION

### A. Coasting

The data indicate that the shock-bang time occurs earlier relative to the main compression burn in long-coast implosions than in short-coast implosions. The interpretation of this observation is that the imploding shell is at a larger radius ( $R_{cm}$ ) during the shock bang for the long-coast implosions. This means that the final rebounding shock, which creates the shock bang, is either faster relative to the implosion velocity or launched earlier for the long-coast pulses.

The shock transit time in the gas (after break-out from the shell) is  $\sim 4$  ns according to HYDRA simulations (see

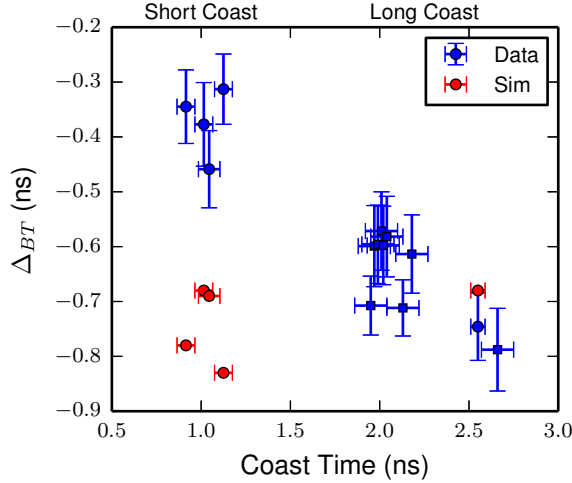


FIG. 17: Estimated difference in time between shock and compression bang, contrasted to simulations, for 2DConA (square) and ConA (round) implosions, which were also probed with in-flight x-ray radiography. The two points at coasting time  $\sim 2.5$  ns show good agreement between the two experimental platforms. Uncertainties are random, with an additional  $\pm 0.11$  ns systematic uncertainty.

Fig. 1a). This can also be estimated using simple models. For example, using the Hugoniot conditions, a shock launched by 100 MBar of pressure at the ablation front propagates through the pre-compressed shell in approximately 450 ps. This shock propagates through the density discontinuity at the inner surface of the shell<sup>38</sup> and spherically converges as a Guderley shock<sup>22</sup> through the initial gas, which takes an additional  $\sim 4.1$  ns. However, at the time when the shock is launched into the gas, the sound speed in the shell  $c = \sqrt{\gamma P/\rho}$  is quite low. For an ideal gas at 100 MBar pressure and density of  $\rho = 20$  g/cc, the speed of sound is only  $\sim 30$   $\mu\text{m}/\text{ns}$  (in the frame of the imploding shell). But since the inward shell fluid velocity at shock breakout is  $\sim 60$   $\mu\text{m}/\text{ns}$  and the shock velocity in the lab frame is  $\sim 150$   $\mu\text{m}/\text{ns}$ , the shock is already effectively decoupled from the driving piston of the ablation front. The coasting dynamics happen later in time and thus cannot directly affect the shock strength in this scenario.

The late-time drive will affect the implosion (shell) trajectory. If the implosion comes in late relative to the shock, the bang-time differential will increase. This could occur, for instance, due to in-flight decompression and deceleration of the shell if the ablation pressure decreases while the shell is still at a large radius. Since the data and simulations are discrepant for the short-coast implosions, this suggests that the late-time drive (during the last ns) is not well modeled in the simulation. This could be related to the drive degradation multipliers required to match implosion data, an uncertainty in radiation trans-

port through the ablated shell material, or an uncertainty in the compressed ablator equation of state.

One potential significance of an earlier shock-bang time is its implications for the deceleration phase of the implosion. Deceleration begins when the rebounding shock (as a heat wave) encounters the incoming shell. The rebound phase can also be calculated using Guderley's solution<sup>22</sup>. For a constant shock strength, an earlier shock-bang time means that the rebounding shock will hit the incoming shell at an earlier time (larger radius) and thus deceleration will begin earlier. This could reduce the compression and final  $\rho R$  of the implosion. Interestingly, data in cryogenic implosions show 25 – 50% higher  $\rho R$  and higher inferred stagnation pressure for short-coast implosions<sup>39,40</sup>. This is consistent with this work's interpretation of the short-coast implosions where the shock dynamics is more amenable to high compression, i.e. later shock-bang time relative to compression.

## B. Hot-spot adiabat

The significance of large variation in shock proton yield can be interpreted in the context of the shock dynamics and hot-spot adiabat. The initial heating of the low-density material at the center of the implosion is from the imploding and rebounding shock, which sets the incipient hot-spot adiabat prior to the onset of deceleration and subsequent  $PdV$  heating of the hot spot. The hot-spot adiabat can be roughly characterized as the ratio of its pressure to the Fermi pressure:

$$\alpha \equiv \frac{P}{P_f} = \frac{n_e k_B T_e + n_i k_B T_i}{\frac{(3\pi^2)^{2/3} \hbar^2}{5m_e} n_e^{5/3}}. \quad (9)$$

The shock preferentially heats ions over electrons<sup>16</sup> and in this Guderley model they are assumed to be uncoupled ( $\tau_{ei}$  long compared to dynamical timescales)<sup>41</sup>.

We can interpret the shock proton yield via a simple model based on the Guderley spherically-imploding shock solution<sup>16,22</sup>. The Guderley model gives hydrodynamic profiles in a self-similar solution as a function of a single shock strength parameter,  $\xi$ . For a single choice of  $\xi$ , the  $\text{D}^3\text{He}$  yield ( $Y$ ) is calculated from:

$$Y = \int f_D f_{3\text{He}} n_i^2 \langle \sigma v \rangle d^3 r dt, \quad (10)$$

where  $f_D$  and  $f_{3\text{He}}$  are the fuel ion fractions and  $\langle \sigma v \rangle$  is the temperature-dependent fusion reactivity. A mass-weighted hot-spot adiabat is also calculated via Eq. 9, evaluated when the rebounding shock encounters the incoming shell material. The shock strength  $\xi$  is then varied to map out a relationship between the proton shock yield and hot-spot adiabat, and this relationship is well described by a power law:

$$\alpha = 2.10 Y^{0.247} + 16.4, \quad (11)$$

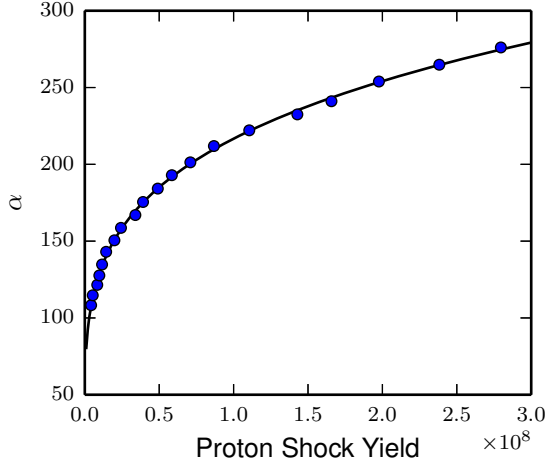


FIG. 18: Inferred hot-spot adiabat ( $\alpha$ ) versus proton shock yield using a Guderley model. Points are at values of  $\xi$  from 250 – 350 (at intervals of 5)  $\mu\text{m}/\text{ns}^{0.688}$ . The solid curve is a power-law fit (see Eq. 10).

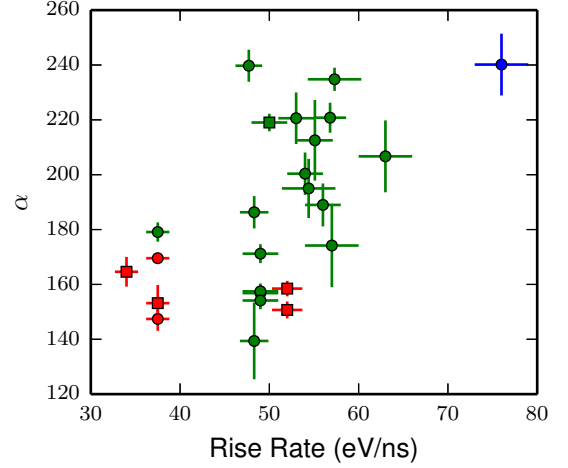


FIG. 20: Modeled adiabat versus rise rate for the same dataset as Fig.14d-f.

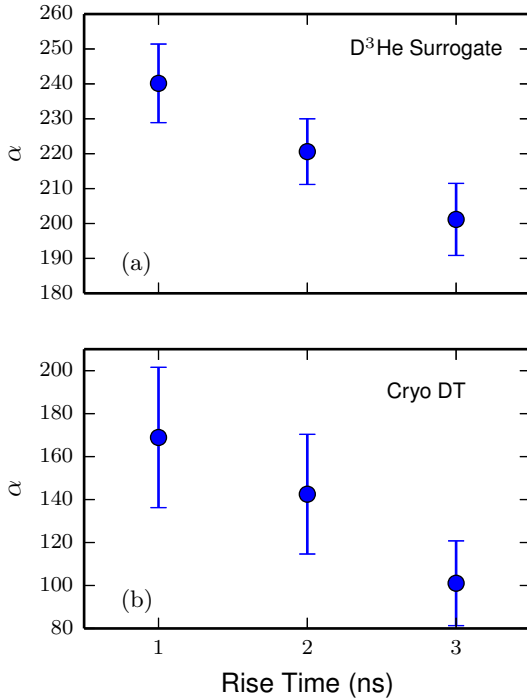


FIG. 19: (a) Modeled adiabat versus rise time for the same dataset as shown in Fig.15. (b) Modeled hot-spot adiabat in cryogenic implosions.

where the coefficients are from a fit to the model results. This relation is shown in Fig. 18.

Using this model, the adiabat can be determined from the yield and thus rise time (see Fig. 19). The hot-spot adiabat increases for faster rise times due to a stronger launched shock. This empirical result can be compared

qualitatively to modeled hot-spot adiabats<sup>42</sup> for cryogenic implosions<sup>40,43</sup>, in which a very similar trend is seen where  $\alpha$  increases from  $\sim 100$  to  $\sim 160$  as the rise time decreases from 3 to 1 ns. The absolute values of  $\alpha$  inferred for these surrogate implosions are expected to be higher than cryogenic implosions, since ablation of low-adiabat ice material in the latter decreases the hot-spot adiabat. Further modeling is required to directly relate surrogate hot-spot adiabat to cryogenic hot-spot adiabat, but this is motivated by the lack of any other direct measurement of the hot-spot adiabat. Additionally, 3-D effects are expected to alter the inferred hot-spot adiabat in cryogenic experiments, so a better understanding of the incipient adiabat and hot-spot formation process may increase our understanding of these 3-D effects.

Inferred values of  $\alpha$  as a function of measured radiation-temperature rise rate are shown for the 30 downselected shots used in Fig. 20, analogous to Fig. 59 of Ref. 40. The factor of  $10\times$  variation in shock proton yield corresponds to  $\sim 75\%$  variation in  $\alpha$ , as seen from the power 0.247 in Eq. 10. For the entire dataset (Fig. 11), a  $35\times$  min-max variation in shock yield is observed, corresponding to a  $\sim 2.4\times$  variation in  $\alpha$ .

## VII. CONCLUSIONS AND FUTURE WORK

The shock dynamics of surrogate implosions at the NIF have been studied. From proton spectroscopy the shock  $\rho R$ , proton yield, and shell radius at shock-bang time are determined using a simple self-consistent 1-D implosion model. The shock  $\rho R$  data show dependence on the coasting time of the implosion, with short-coast implosions having higher shock  $\rho R$ . The proton shock yield data show a clear dependence on the laser-pulse rise time, and possibly peak power. Using the inferred center-of-mass radius and in-flight x-ray radiography, a shock-bang

time is estimated. The short-coast implosions are observed to have significantly smaller differences between the shock- and compression-bang times than the long-coast implosions. This could be due to uncertainties in modeling the late-time drive on the capsule, which is the primary difference between short- and long-coast experiments. An earlier shock-bang time in long-coast implosions could reduce compressibility due to an earlier onset of deceleration; in cryogenic implosions lower compression  $\rho R$  is measured in long-coast implosions. Further, the large variation in shock yield indicates a variation in post-shock temperature and thus adiabat of the incipient hot-spot material. A model is introduced to relate the proton shock yield to adiabat; this analysis suggests an increase in hot-spot adiabat of up to  $2\times$  in fast-rise implosions, potentially reducing compressibility.

Future campaigns could be conducted to more systematically study the effect of coasting time, rise time, and peak power on shock dynamics, or to study the effect of hohlraum material (not addressed in this work). Implementation of a diagnostic for direct measurements of the shock-bang time, which is in progress<sup>44</sup>, will be a direct and higher-precision diagnostic of the differential bang time. This new diagnostic will be used to further investigate the discrepancy observed in this work between the model-inferred differential bang time and radiation-hydrodynamics simulations (Fig. 17). Accurate modeling of the shock phase in ignition experiments essentially sets the initial conditions for hot-spot formation. The observed inaccuracies in standard hydrodynamic models for the surrogate implosions strongly suggest that the ignition experiments are not being accurately modeled. For example, non-hydrodynamic kinetic or two-fluid effects not included in the simulations could be important<sup>28,29</sup>, and are potentially even more substantial in cryogenic targets due to a  $20\times$  lower initial gas density.

## ACKNOWLEDGMENTS

We thank the operations crews and engineering staff at NIF for supporting these experiments, and M. McKernan, M. Cairel, and M. Valadez for their work processing the CR-39.

This work is part of the first author's Ph.D. thesis, and was supported in part by the U.S. DoE (Grant No. DE-NA0001857, DE-FC52-08NA28752), LLNL (No. B597367), LLE (No. 415935-G), the Fusion Science Center at the University of Rochester (No. 524431), and the National Laser Users Facility (No. DE-NA0002035). This material is based upon work supported by the National Science Foundation Graduate Research Fellowship Program under Grant No. 1122374.

Prepared in part by LLNL under Contract DE-AC52-07NA27344.

## Appendix A: Sample Analysis

For the sample spectrum shown in Fig. 4, the results of the spectral analysis and subsequent  $\rho R$  modeling are shown in Table I.

TABLE I: Results from the analysis of the D<sup>3</sup>He proton spectrum for N101004-002-999 on DIM 90-78.

Quantity	Value	$\pm$ random	$\pm$ systematic <sup>a</sup>	$\pm$ model
Energy (MeV)	11.34	0.10	0.10	
$\sigma$ (MeV)	0.43	0.10	n/a	
Yield	$8.71 \times 10^7$	$0.94 \times 10^7$	n/a	
$\rho R$ (mg/cm <sup>2</sup> )	96.0	3.1	6.1	5.3
$R_{cm}$ ( $\mu$ m)	242	5	35	34

<sup>a</sup> Includes model uncertainty

Error bars are  $1\sigma$ . For the proton energy, the systematic uncertainty primarily comes from the energy calibration of the WRFs<sup>45</sup>, and random uncertainty comes from a combination of factors such as the hohlraum, variation in CR-39 properties, and statistical uncertainty. For the yield and line width, there are no systematic uncertainties, and the random uncertainties are primarily variation in CR-39 and statistics.

The energy uncertainties propagate to the modeled quantities  $\rho R$  and  $R_{cm}$ . The systematic uncertainties for these quantities also include, and are dominated by, the modeling uncertainty. The model uncertainty is also listed separately in Table I.

## Appendix B: Hohlraum Corrections

WRFs fielded on the equator always look through the hohlraum wall in indirect-drive experiments at the NIF. The large patches that would be required to give a clear line of sight for the 4 WRFs that are fielded on DIM 90-78 would unacceptably impact the implosion performance.

In addition to the high-Z hohlraum wall, which is made of Au or DU, there is a Thermo-Mechanical Package (TMP) made of thin aluminum. For most experiments, the hohlraum wall profile is defined by engineering drawings, and the energy correction due to the hohlraum wall is done by calculating the average thickness intercepted by the WRF line-of-sight. The uncertainties in hohlraum thickness ( $\pm 1 \mu$ m for the hohlraum wall, and  $\pm 3 \mu$ m for the TMP) are standard tolerances, and these uncertainties are propagated through the analysis. In this case, the hohlraum uncertainty contributes  $\pm 56$  keV of uncertainty to the final determined energy.

The actual energy correction is applied to the entire spectrum, as shown in Fig. 21 by shifting each energy using cold-matter stopping powers<sup>46</sup>. The use of



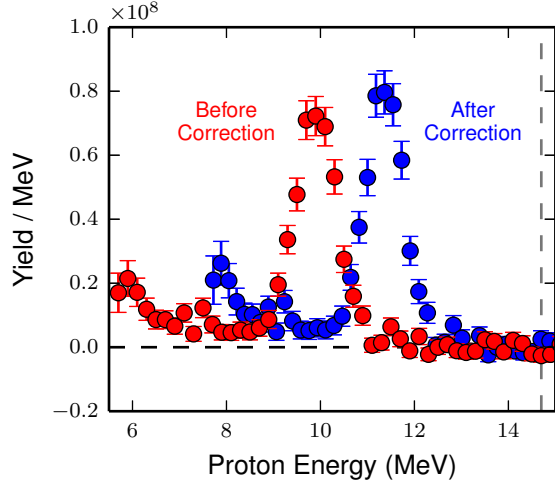


FIG. 21: Sample  $D^3He$  proton spectrum from NIF shot N101004-002-999, measured on the equator (DIM 90-78) before (red) and after (blue) hohlraum correction. In this case, the hohlraum thickness was  $24.2 \pm 1 \mu\text{m}$  of Au and  $74.1 \pm 3 \mu\text{m}$  of Al.

cold-matter stopping power in the hohlraum wall is a good approximation and has been checked against fully-integrated radiation-hydrodynamics hohlraum calculations. Because of the non-linearity in stopping power with proton energy, lower proton energies experience more downshift than higher energy protons, which has an ‘accordion’ effect on the spectrum, though a Gaussian shape is maintained for the energies in this work ( $\gtrsim 5$  MeV).

For some hohlraum designs a ‘bump’ feature is present in the WRF line of sight. During the laser pulse a shock passes through the wall, and in the bump material flows laterally out of the line of sight. This situation is calculated with 2-D radiation-hydrodynamic simulations, and the wall thickness is corrected based on these simulations.

### Appendix C: Implosion Model Parameterization

Typical parameters and assumptions in the 1-D implosion model are shown in Table II with uncertainties. The first six (shell material, inner and outer radius, fuel pressure, and fuel fill) are determined from a database of shot setup parameters. The values shown in the table are typical numbers. For the shell material, the ablator dopant (Ge or Si) is included, though the dopant level ( $\sim 1\%$ ) has negligible effect on the inferred quantities. The following 10 parameters are treated as assumptions in the model and characterize the in-flight properties of the implosion. The ablated mass density profile (defined by  $\rho_{\text{max}}$ ,  $\rho_{\text{min}}$ , and  $\lambda$ ) is given in Eq. 7.

In the table we also give the resulting uncertainties in  $\rho R$  for shot N101004 (see also Fig. 4 and Appendix

TABLE II: Typical values used in the model

Parameter	Value	$\pm$	N101004 $\pm \rho R$ mg/cm <sup>2</sup>
<i>Initial Conditions</i>			
Shell Material <sup>a</sup>	CH	n/a	n/a
Inner Radius ( $\mu\text{m}$ )	900	5	0.05
Outer Radius ( $\mu\text{m}$ )	1100	5	0.0
Fuel fill (mg/cm <sup>3</sup> )	6.3	0.1	0.06
Fuel D Fraction	0.3	0.0	0
Fuel $^3\text{He}$ fraction	0.7	0.0	0
<i>In-flight Assumptions</i>			
Gas T (keV)	3	2	4.43
Mix T (keV)	0.5	0.2	0.23
Shell T (keV)	0.2	0.1	0.23
Ablated mass T (keV)	0.3	0.1	0.01
$\rho_{\text{max}}$ (g/cc)	1.5	0.5	1.02
$\rho_{\text{min}}$ (g/cc)	0.1	0.05	1.25
$\lambda$ ( $\mu\text{m}$ )	70	30	1.25
Mix Fraction <sup>b</sup>	0.5%	0.5%	0.16
Shell Thickness <sup>c</sup> ( $\mu\text{m}$ )	40	10	1.65
Mass Remaining <sup>d</sup>	17.5%	5%	1.10

<sup>a</sup> Dopant type and level included; typically 1.084 g/cc, 57.2% H, 42.3% C, and 0.5% O atomic plus mid-Z dopant (Ge or Si).

<sup>b</sup> Percentage of the initial shell mass

<sup>c</sup> Full width of the in-flight shell

<sup>d</sup> For surrogate implosions, the quoted mass remaining includes the surrogate mass of CH

A) resulting directly from the uncertainties in the model parameters. The dominant sources are the uncertainty in fuel temperature, ablated mass density profile (collectively from  $\rho_{\text{max}}$ ,  $\rho_{\text{min}}$ , and  $\lambda$ ), in-flight shell thickness, and mass remaining. The other sources of uncertainty are negligible ( $\ll 1$  mg/cm<sup>2</sup>).

A mix model was added to this framework to evaluate the potential impact of mix on the proton  $dE/dx$ , primarily in the fuel where the electron temperature can be high. The modeled mix is a uniform CH mix into the fuel specified by the amount of the initial shell mass which is mixed. Even assuming an implausibly large variation in mix (0 – 1% of the initial shell) causes only a 0.3 mg/cm<sup>2</sup> difference in inferred  $\rho R$ ; since 1% mix corresponds to a mix mass of 25  $\mu\text{g}$ , about  $\sim 10\times$  higher than the worst observed<sup>47</sup>, we conclude that mix is unimportant for shock proton spectroscopy.

The primary effect of the changing density and temperature in the three regions is variation in the stopping power, which is shown in Fig. 22. The higher temperature in the fuel leads to a much higher energy Bragg peak. At high energy, the stopping power in the shell is lower than in the fuel or the ablated mass due to the higher density in the shell (leading to a smaller  $\log \Lambda$ ).



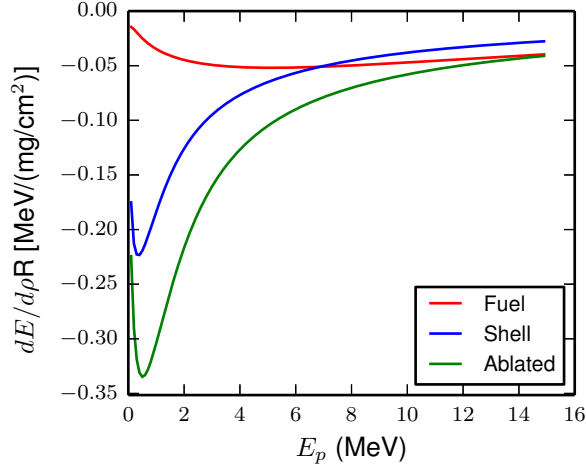


FIG. 22: Stopping power for the three components of the implosion model: fuel, shell, and ablated mass.

#### Appendix D: Extension of the Implosion Model to 2- and 3-D

A simple extension of the implosion model to 2- and 3-D is essential for analysis of asymmetries observed between multiple detectors in these implosions, enabling the work presented in Ref. 19. An asymmetry is modeled as Legendre modes in the shape of the imploding shell:

$$R_{cm}(\theta, \phi) = \bar{R} \left[ 1 + \Delta \times \sqrt{\frac{2\ell+1}{4\pi}} \frac{(\ell-m)!}{(\ell+m)!} e^{im\phi} P_\ell^m(\cos\theta) \right], \quad (\text{D1})$$

where  $\theta$  and  $\phi$  are the polar and azimuthal angles, respectively,  $\bar{R}$  is the unperturbed shell radius,  $\Delta$  is the fractional asymmetry amplitude, and  $P_\ell^m$  is an associated Legendre polynomial.

From the 1-D model presented in this paper, we have  $\rho R(R_{cm})$ . Areal density asymmetries in 2- or 3-D can thus be modeled as the convolution of  $R_{cm}(\theta, \phi)$  and  $\rho R(R_{cm})$  giving  $\rho R(\theta, \phi, \bar{R}, \Delta, \ell, m)$ . The data points, each with their own coordinates  $(\theta, \phi)$ , are then fit using this convolution, where  $\Delta$  and  $\bar{R}$  are free parameters and  $\ell, m$  are chosen.

An example of this analysis is shown in Fig. 23 for shot N101218-002-999. In this case a  $P_2$  mode is assumed ( $\ell = 2, m = 0$ ). The best fit parameters are  $\bar{R} = 250 \pm 2 \mu\text{m}$  and  $\Delta = -0.21 \pm 0.02$ . The error bars are due to random/statistical errors only, excluding systematic detector calibration uncertainties and model uncertainties.

For the ConA2D implosions (see next section) in-flight 2-D x-ray radiography is used to measure the symmetry. Unfortunately the radiography requires large patches on the hohlraum wall, which induce a known  $m = 2$  azimuthal asymmetry. This asymmetry is roughly aligned with the WRF equatorial line of sight, leading to an un-

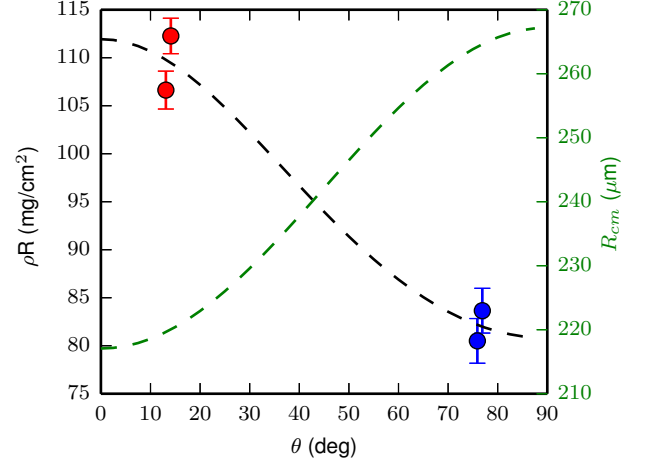


FIG. 23:  $\rho R$  asymmetry analysis ( $\ell = 2, m = 0$ ) for shot N101218-002-999, which had an usually large observed asymmetry. The polar (red) and equatorial (blue) data are shown with random/statistical errors only. The fit is shown as  $\rho R(\theta)$  and  $R_{cm}(\theta)$  (right axis).

constrained problem between the modes  $\ell = 2$  and  $m = 2$  plus modes such as  $\ell = 4$ . To address this issue we use the radiography-measured mode amplitudes for the  $\ell = 2$  and  $\ell = 4$  and fit the amplitude of the  $m = 2$  mode:

$$R_{cm}(\theta, \phi) = \bar{R} \left[ 1 + \Delta_{m=2} \sin\theta \cos(2\phi + \phi_0) + \Delta_{\ell=2} \times \sqrt{\frac{5}{4\pi}} P_2^0(\cos\theta) + \Delta_{\ell=4} \times \sqrt{\frac{9}{4\pi}} P_4^0(\cos\theta) \right], \quad (\text{D2})$$

where  $\Delta_{m=2}$  is the free parameter and  $\phi_0$  is taken as aligned with the equatorial line of sight ( $78^\circ$ ). The polar amplitudes  $\Delta_{\ell=2}$  and  $\Delta_{\ell=4}$  are determined from x-ray radiography.

#### Appendix E: Down-selected Data Summary

A summary of the data used in the shock dynamics analysis is shown in Table III.

- <sup>1</sup>J. Nuckolls, L. Wood, A. Thiessen, and G. Zimmerman, *Nature* **239**, 139 (1972).
- <sup>2</sup>J. Lindl, *Physics of Plasmas* **2**, 3933 (1995).
- <sup>3</sup>G. Miller, E. Moses, and C. Wuest, *Nuclear Fusion* **44**, S228 (2004).
- <sup>4</sup>O. Landen *et al.*, *Physics of Plasmas* **17**, 056301 (2010).
- <sup>5</sup>G. Kyrala *et al.*, *Rev. of Sci. Instrum.* **81**, 10E316 (2010).
- <sup>6</sup>G. Kyrala *et al.*, *Physics of Plasmas* **18**, 056307 (2011).
- <sup>7</sup>D. Hicks, B. Spears, D. Braun, R. Olson, C. Sorce, P. Celliers, G. Collins, and O. Landen, *Physics of Plasmas* **17**, 102703 (2010).

TABLE III: Data summary of shots used in the shock dynamics analysis

Shot	Type	Hohlraum	Laser Energy (MJ)	Effective Power (TW)	Absorption	Rise Time (ns)	Coast Time (ns)	Average $\rho R$ (mg/cm <sup>2</sup> )	Equatorial Shock Yield	$R_{cm}$ ( $\mu m$ )	$\Delta_{BT}$ (ns)
N110728-001-999	Symcap	Au	1.39 $\pm$ 0.03	368 $\pm$ 7	0.83 $\pm$ 0.03	2	1.94 $\pm$ 0.11	91 $\pm$ 13	(3.8 $\pm$ 1.3) $\times$ 10 <sup>7</sup>	247 $\pm$ 36	
N111007-002-999	ConvAblW	Au	1.29 $\pm$ 0.02	350 $\pm$ 7	0.84 $\pm$ 0.03	2	2.46 $\pm$ 0.04	80 $\pm$ 6	(7.1 $\pm$ 1.1) $\times$ 10 <sup>7</sup>	269 $\pm$ 40	
N111011-004-999	ConvAbl	Au	1.27 $\pm$ 0.02	346 $\pm$ 7	0.86 $\pm$ 0.03	2	2.55 $\pm$ 0.04	82 $\pm$ 11	(1.1 $\pm$ 0.1) $\times$ 10 <sup>8</sup>	265 $\pm$ 40	-0.75 $\pm$ 0.16
N111013-001-999	Symcap	Au	1.24 $\pm$ 0.02	367 $\pm$ 7	0.84 $\pm$ 0.03	2	2.52 $\pm$ 0.05	88 $\pm$ 11	(6.3 $\pm$ 1.4) $\times$ 10 <sup>7</sup>	252 $\pm$ 38	
N111014-001-999	Symcap	Au	1.26 $\pm$ 0.02	368 $\pm$ 7	0.84 $\pm$ 0.03	2	2.44 $\pm$ 0.05	87 $\pm$ 6	(1.4 $\pm$ 0.1) $\times$ 10 <sup>8</sup>	255 $\pm$ 40	
N111106-002-999	Symcap	Au	1.27 $\pm$ 0.02	365 $\pm$ 7	0.83 $\pm$ 0.03	2	2.48 $\pm$ 0.08	84 $\pm$ 12	(9.2 $\pm$ 2.6) $\times$ 10 <sup>7</sup>	260 $\pm$ 40	
N111109-002-999	Symcap	Au	1.26 $\pm$ 0.03	370 $\pm$ 7	0.86 $\pm$ 0.03	2	2.43 $\pm$ 0.08	86 $\pm$ 12	(8.1 $\pm$ 2.1) $\times$ 10 <sup>7</sup>	256 $\pm$ 39	
N111119-002-999	ConvAblW	Au	1.17 $\pm$ 0.02	342 $\pm$ 7	0.85 $\pm$ 0.03	2	2.51 $\pm$ 0.04	77 $\pm$ 10	(5.5 $\pm$ 0.9) $\times$ 10 <sup>7</sup>	277 $\pm$ 43	
N111120-002-999	Symcap	Au	1.50 $\pm$ 0.03	375 $\pm$ 7	0.84 $\pm$ 0.03	2	1.74 $\pm$ 0.08	94 $\pm$ 12	(1.6 $\pm$ 0.2) $\times$ 10 <sup>8</sup>	242 $\pm$ 36	
N111219-001-999	ConvAblW	Au	1.41 $\pm$ 0.02	353 $\pm$ 7	0.85 $\pm$ 0.03	2	1.95 $\pm$ 0.10	92 $\pm$ 12	(1.1 $\pm$ 0.2) $\times$ 10 <sup>8</sup>	245 $\pm$ 38	
N111220-002-999	ConvAblW	Au	1.41 $\pm$ 0.03	352 $\pm$ 7	0.84 $\pm$ 0.03	1	2.03 $\pm$ 0.10	89 $\pm$ 12	(1.6 $\pm$ 0.3) $\times$ 10 <sup>8</sup>	251 $\pm$ 38	
N120408-001-999	ConvAbl	U	1.52 $\pm$ 0.03	292 $\pm$ 5	0.81 $\pm$ 0.03	3	0.92 $\pm$ 0.05	139 $\pm$ 10	(3.0 $\pm$ 0.4) $\times$ 10 <sup>7</sup>	191 $\pm$ 28	-0.34 $\pm$ 0.12
N120409-001-999	ConvAbl	U	1.65 $\pm$ 0.03	350 $\pm$ 7	0.86 $\pm$ 0.02	2	1.01 $\pm$ 0.05	137 $\pm$ 9	(1.0 $\pm$ 0.1) $\times$ 10 <sup>8</sup>	193 $\pm$ 29	-0.38 $\pm$ 0.13
N120418-001-999	ConvAbl	U	1.70 $\pm$ 0.03	336 $\pm$ 6	0.82 $\pm$ 0.03	3	1.12 $\pm$ 0.05	152 $\pm$ 10	(2.1 $\pm$ 0.4) $\times$ 10 <sup>7</sup>	181 $\pm$ 29	-0.31 $\pm$ 0.13
N120421-006-999	ConvAbl	Au	1.63 $\pm$ 0.03	306 $\pm$ 6	0.85 $\pm$ 0.03	3	1.04 $\pm$ 0.06	133 $\pm$ 9	(3.4 $\pm$ 0.1) $\times$ 10 <sup>7</sup>	196 $\pm$ 28	-0.46 $\pm$ 0.13
N120629-002-999	ConvAblW	U	1.34 $\pm$ 0.03	297 $\pm$ 6	0.84 $\pm$ 0.02	3	1.61 $\pm$ 0.06	138 $\pm$ 10	(2.5 $\pm$ 0.2) $\times$ 10 <sup>7</sup>	191 $\pm$ 27	
N120709-003-999	ConvAblW	Au	1.57 $\pm$ 0.03	298 $\pm$ 6	0.85 $\pm$ 0.03	3	1.15 $\pm$ 0.06	137 $\pm$ 9	(1.8 $\pm$ 0.2) $\times$ 10 <sup>7</sup>	192 $\pm$ 28	
N120726-003-999	Symcap	Au	1.37 $\pm$ 0.03	345 $\pm$ 7	0.84 $\pm$ 0.02	2	2.31 $\pm$ 0.06	105 $\pm$ 7	(4.3 $\pm$ 0.3) $\times$ 10 <sup>7</sup>	226 $\pm$ 36	
N120909-001-999	Symcap	Au	1.43 $\pm$ 0.03	370 $\pm$ 7	0.86 $\pm$ 0.02	2	2.00 $\pm$ 0.05	81 $\pm$ 13	(1.4 $\pm$ 0.6) $\times$ 10 <sup>7</sup>	266 $\pm$ 42	
N120910-001-999	Symcap	Au	1.46 $\pm$ 0.03	376 $\pm$ 8	0.86 $\pm$ 0.02	2	2.06 $\pm$ 0.05	92 $\pm$ 6	(5.1 $\pm$ 0.7) $\times$ 10 <sup>7</sup>	245 $\pm$ 38	
N121008-002-999	ConvAblW	U	1.28 $\pm$ 0.03	290 $\pm$ 5	0.86 $\pm$ 0.02	3	1.68 $\pm$ 0.09	149 $\pm$ 11	(2.0 $\pm$ 0.2) $\times$ 10 <sup>7</sup>	183 $\pm$ 26	
N121202-001-999	ConvAbl2D	Au	1.28 $\pm$ 0.03	315 $\pm$ 7	0.86 $\pm$ 0.02	2	1.97 $\pm$ 0.09	110 $\pm$ 8	(2.4 $\pm$ 0.2) $\times$ 10 <sup>7</sup>	219 $\pm$ 31	-0.60 $\pm$ 0.13
N121210-001-999	ConvAbl2D	Au	1.28 $\pm$ 0.03	315 $\pm$ 7	0.86 $\pm$ 0.02	2	1.99 $\pm$ 0.09	110 $\pm$ 7	(2.4 $\pm$ 0.2) $\times$ 10 <sup>7</sup>	219 $\pm$ 31	-0.60 $\pm$ 0.13
N121218-004-999	ConvAbl2D	Au	1.29 $\pm$ 0.03	317 $\pm$ 7	0.87 $\pm$ 0.02	2	2.02 $\pm$ 0.09	107 $\pm$ 7	(2.2 $\pm$ 0.2) $\times$ 10 <sup>7</sup>	223 $\pm$ 32	-0.60 $\pm$ 0.13
N121219-001-999	ConvAbl2D	Au	1.29 $\pm$ 0.03	302 $\pm$ 7	0.87 $\pm$ 0.02	2	2.01 $\pm$ 0.09	119 $\pm$ 8	(3.5 $\pm$ 0.3) $\times$ 10 <sup>7</sup>	209 $\pm$ 31	-0.57 $\pm$ 0.13
N130211-003-999	ConvAbl2D	Au	1.28 $\pm$ 0.03	325 $\pm$ 6	0.91 $\pm$ 0.03	2	2.04 $\pm$ 0.09	110 $\pm$ 8	(5.5 $\pm$ 0.3) $\times$ 10 <sup>7</sup>	220 $\pm$ 32	-0.58 $\pm$ 0.13
N130212-001-999	ConvAbl2D	Au	1.27 $\pm$ 0.03	321 $\pm$ 6	0.90 $\pm$ 0.03	2	2.18 $\pm$ 0.09	100 $\pm$ 7	(6.2 $\pm$ 0.5) $\times$ 10 <sup>7</sup>	233 $\pm$ 33	-0.61 $\pm$ 0.13
N130213-002-999	ConvAbl2D	Au	0.96 $\pm$ 0.02	222 $\pm$ 4	0.91 $\pm$ 0.03	2	2.66 $\pm$ 0.09	105 $\pm$ 8	(8.7 $\pm$ 0.8) $\times$ 10 <sup>6</sup>	226 $\pm$ 32	-0.79 $\pm$ 0.19
N130226-002-999	ConvAbl2D	Au	1.28 $\pm$ 0.02	323 $\pm$ 5	0.90 $\pm$ 0.03	2	1.95 $\pm$ 0.09	100 $\pm$ 7	(5.0 $\pm$ 0.5) $\times$ 10 <sup>7</sup>	233 $\pm$ 34	-0.71 $\pm$ 0.13
N130227-002-999	ConvAbl2D	Au	1.28 $\pm$ 0.02	322 $\pm$ 4	0.89 $\pm$ 0.03	2	2.13 $\pm$ 0.09	98 $\pm$ 7	(6.4 $\pm$ 0.6) $\times$ 10 <sup>7</sup>	236 $\pm$ 33	-0.71 $\pm$ 0.12

- <sup>8</sup>D. G. Hicks *et al.*, *Physics of Plasmas* (1994-present) **19**, 122702 (2012).
- <sup>9</sup>G. Zimmerman and W. Kruer, *Controlled Fusion* **2**, 51 (1975).
- <sup>10</sup>S. Haan *et al.*, *Physics of Plasmas* **2**, 2480 (1995).
- <sup>11</sup>M. Marinak, G. Kerbel, N. Gentile, O. Jones, D. Munro, S. Pol-laine, T. Dittrich, and S. Haan, *Physics of Plasmas* **8**, 2275 (2001).
- <sup>12</sup>D. G. Hicks, *Charged-Particle Spectroscopy: A New Window on Inertial Confinement Fusion* (Massachusetts Institute of Tech-nology, 1999).
- <sup>13</sup>R. Petrasso *et al.*, *Physical Review Letters* **90**, 95002 (2003).
- <sup>14</sup>C. K. Li, F. H. Sguin, J. A. Frenje, R. D. Petrasso, R. Rygg, S. Kurebayashi, B. Schwartz, R. L. Keck, J. A. Delettretz, J. M. Soures, P. W. McKenty, V. N. Goncharov, J. P. Knauer, F. J. Marshall, D. D. Meyerhofer, P. B. Radha, S. P. Regan, T. C. Sangster, W. Seka, and C. Stoeckl, *Physics of Plasmas* (1994-present) **10**, 1919 (2003).
- <sup>15</sup>J. A. Frenje, C. K. Li, F. H. Sguin, J. Deciantis, S. Kurebayashi, J. R. Rygg, R. D. Petrasso, J. Delettretz, V. Y. Glebov, C. Stoeckl, F. J. Marshall, D. D. Meyerhofer, T. C. Sangster, V. A. Smalyuk, and J. M. Soures, *Physics of Plasmas* **11**, 2798 (2004).
- <sup>16</sup>J. R. Rygg, *Shock Convergence and Mix Dynamics in Iner-tial Confinement Fusion* (Massachusetts Institute of Technology, 2006).
- <sup>17</sup>T. Boehly, D. Brown, R. Craxton, R. Keck, J. Knauer, J. Kelly, T. Kessler, S. Kumpan, S. Loucks, S. Letzring, F. Marshall, R. McCrory, S. Morse, W. Seka, J. Soures, and C. Verdon, *Optics Communications* **133**, 495 (1997).
- <sup>18</sup>A. B. Zylstra, J. A. Frenje, F. H. Séguin, M. J. Rosenberg, H. G. Rinderknecht, M. G. Johnson, D. T. Casey, N. Sinenian, M. J.-E. Manuel, C. J. Waugh, H. W. Sio, C. K. Li, R. D. Petrasso, S. Friedrich, K. Knittel, R. Bionta, M. McKernan, D. Calla-han, G. W. Collins, E. Dewald, T. Döppner, M. J. Edwards, S. Glenzer, D. G. Hicks, O. L. Landen, R. London, A. Mackin-non, N. Meezan, R. R. Prasad, J. Ralph, M. Richardson, J. R. Rygg, S. Sepke, S. Weber, R. Zacharias, E. Moses, J. Kilkenny, A. Nikroo, T. C. Sangster, V. Glebov, C. Stoeckl, R. Olson, R. J. Leeper, J. Kline, G. Kyralla, and D. Wilson, *Review of Scientific Instruments* **83**, 10D901 (2012).
- <sup>19</sup>A. B. Zylstra *et al.*, to be submitted to *Phys. Rev. Lett.* (2013).
- <sup>20</sup>The proton velocity is high relative to the electron thermal ve-locity in these regimes, so electron stopping dominates.
- <sup>21</sup>C. Li and R. Petrasso, *Physical Review Letters* **70**, 3059 (1993).
- <sup>22</sup>G. Guderley, *Luftfahrtforsch* **19**, 302 (1942).
- <sup>23</sup>P. M. Celliers, D. K. Bradley, G. W. Collins, D. G. Hicks, T. R. Boehly, and W. J. Armstrong, *Review of Scientific Instruments* **75**, 4916 (2004).
- <sup>24</sup>H. F. Robey, P. M. Celliers, J. L. Kline, A. J. Mackinnon, T. R. Boehly, O. L. Landen, J. H. Eggert, D. Hicks, S. Le Pape, D. R. Farley, M. W. Bowers, K. G. Krauter, D. H. Munro, O. S. Jones, J. L. Milovich, D. Clark, B. K. Spears, R. P. J. Town, S. W. Haan, S. Dixit, M. B. Schneider, E. L. Dewald, K. Widmann, J. D. Moody, T. D. Döppner, H. B. Radousky, A. Nikroo, J. J. Kroll, A. V. Hamza, J. B. Horner, S. D. Bhandarkar, E. Dzenitis, E. Alger, E. Giraldez, C. Castro, K. Moreno, C. Haynam, K. N. LaFortune, C. Widmayer, M. Shaw, K. Jancaitis, T. Parham, D. M. Holunga, C. F. Walters, B. Haid, T. Malsbury, D. Trum-mer, K. R. Coffee, B. Burr, L. V. Berzins, C. Choate, S. J. Brere-ton, S. Azevedo, H. Chandrasekaran, S. Glenzer, J. A. Caggiano, J. P. Knauer, J. A. Frenje, D. T. Casey, M. Gatu Johnson, F. H. Séguin, B. K. Young, M. J. Edwards, B. M. Van Wonerghem, J. Kilkenny, B. J. MacGowan, J. Atherton, J. D. Lindl, D. D. Meyerhofer, and E. Moses, *Phys. Rev. Lett.* **108**, 215004 (2012).
- <sup>25</sup>H. F. Robey, J. D. Moody, P. M. Celliers, J. S. Ross, J. Ralph, S. Le Pape, L. Berzak Hopkins, T. Parham, J. Sater, E. R. Mapoles, D. M. Holunga, C. F. Walters, B. J. Haid, B. J. Koziowski, R. J. Dylla-Spears, K. G. Krauter, G. Frieders, G. Ross, M. W. Bowers, D. J. Strozzi, B. E. Yoxall, A. V. Hamza, B. Dzenitis, S. D. Bhandarkar, B. Young, B. M. Van Won-terghem, L. J. Atherton, O. L. Landen, M. J. Edwards, and T. R. Boehly, *Phys. Rev. Lett.* **111**, 065003 (2013).
- <sup>26</sup>J. D. Moody, D. A. Callahan, D. E. Hinkel, P. A. Amendt, K. L. Baker, D. Bradley, P. M. Celliers, E. L. Dewald, L. Di-vo, T. Döppner, D. C. Eder, M. J. Edwards, O. Jones, S. W. Haan, D. Ho, L. B. Hopkins, N. Izumi, D. Kalantar, R. L. Kauff-man, J. D. Kilkenny, O. Landen, B. Lasinski, S. LePape, T. Ma, B. J. MacGowan, S. A. MacLaren, A. J. Mackinnon, D. Meeker, N. Meezan, P. Michel, J. L. Milovich, D. Munro, A. E. Pak, M. Rosen, J. Ralph, H. F. Robey, J. S. Ross, M. B. Schnei-der, D. Strozzi, E. Storm, C. Thomas, R. P. J. Town, K. L. Widmann, J. Kline, G. Kyralla, A. Nikroo, T. Boehly, A. S. Moore, and S. H. Glenzer, *Physics of Plasmas* **21**, 056317 (2014), <http://dx.doi.org/10.1063/1.4876966>.
- <sup>27</sup>R. P. J. Town, D. K. Bradley, A. Kritcher, O. S. Jones, J. R. Rygg, R. Tommasini, M. Barrios, L. R. Benedetti, L. F. Berzak Hopkins, P. M. Celliers, T. Döppner, E. L. Dewald, D. C. Eder, J. E. Field, S. M. Glenn, N. Izumi, S. W. Haan, S. F. Khan, J. L. Kline, G. A. Kyralla, T. Ma, J. L. Milovich, J. D. Moody, S. R. Nagel, A. Pak, J. L. Peterson, H. F. Robey, J. S. Ross, R. H. H. Scott, B. K. Spears, M. J. Edwards, J. D. Kilkenny, and O. L. Landen, *Physics of Plasmas* (1994-present) **21**, 056313 (2014), <http://dx.doi.org/10.1063/1.4876609>.
- <sup>28</sup>M. J. Rosenberg, H. G. Rinderknecht, N. M. Hoffman, P. A. Amendt, S. Atzeni, A. B. Zylstra, C. K. Li, F. H. Séguin, H. Sio, M. G. Johnson, J. A. Frenje, R. D. Petrasso, V. Y. Glebov, C. Stoeckl, W. Seka, F. J. Marshall, J. A. Delettretz, T. C. Sang-ster, R. Betti, V. N. Goncharov, D. D. Meyerhofer, S. Skup-sky, C. Bellei, J. Pino, S. C. Wilks, G. Kagan, K. Molvig, and A. Nikroo, *Phys. Rev. Lett.* **112**, 185001 (2014).
- <sup>29</sup>H. G. Rinderknecht, H. Sio, C. K. Li, A. B. Zylstra, M. J. Rosenberg, P. Amendt, J. Delettretz, C. Bellei, J. A. Frenje, M. Gatu Johnson, F. H. Séguin, R. D. Petrasso, R. Betti, V. Y. Glebov, D. D. Meyerhofer, T. C. Sangster, C. Stoeckl, O. Lan-den, V. A. Smalyuk, S. Wilks, A. Greenwood, and A. Nikroo, *Phys. Rev. Lett.* **112**, 135001 (2014).
- <sup>30</sup>The thicknesses of the in-flight shell can change depending on the laser drive. In ‘short-coast’ implosions the laser drive is on for a longer time, whereas ‘long-coast’ implosions can have shell decompression due to time-truncated drive. However, the model-ing reveals that this effect is not significant for interpreting this data, since the shell decompression does not significantly affect the  $\rho R$  while the shell is at  $R_{cm} \sim 250\mu\text{m}$ .
- <sup>31</sup>F. Séguin *et al.*, *Review of Scientific Instruments* **74**, 975 (2003).
- <sup>32</sup>F. H. Séguin, N. Sinenian, M. Rosenberg, A. Zylstra, M. J.-E. Manuel, H. Sio, C. Waugh, H. G. Rinderknecht, M. G. Johnson, J. Frenje, C. K. Li, R. Petrasso, T. C. Sangster, and S. Roberts, *Review of Scientific Instruments* **83**, 10D908 (2012).
- <sup>33</sup>W. J. Hibbard *et al.*, *Rev. Sci. Instrum.* **72**, 530 (2001).
- <sup>34</sup>C. Li *et al.*, *Physical Review Letters* **102**, 205001 (2009).
- <sup>35</sup>C. Li *et al.*, *Science* **327**, 1231 (2010).
- <sup>36</sup>C. K. Li, A. B. Zylstra, J. A. Frenje, F. H. Sguin, N. Sinenian, R. D. Petrasso, P. A. Amendt, R. Bionta, S. Friedrich, G. W. Collins, E. Dewald, T. Döppner, S. H. Glenzer, D. G. Hicks, O. L. Landen, J. D. Kilkenny, A. J. Mackinnon, N. Meezan, J. Ralph, J. R. Rygg, J. Kline, and G. Kyralla, *New Journal of Physics* **15**, 025040 (2013).
- <sup>37</sup>J. R. Rygg, O. S. Jones, J. E. Field, M. A. Barrios, L. R. Benedetti, G. W. Collins, D. C. Eder, M. J. Edwards, J. L. Kline, J. J. Kroll, O. L. Landen, T. Ma, A. Pak, J. L. Peterson, K. Ra-man, R. P. J. Town, and D. K. Bradley, *Phys. Rev. Lett.* **112**, 195001 (2014).
- <sup>38</sup>R. Drake, *High-Energy-Density-Physics* (Springer, 2006).
- <sup>39</sup>M. J. Edwards, P. K. Patel, J. D. Lindl, L. J. Atherton, S. H. Glenzer, S. W. Haan, J. D. Kilkenny, O. L. Landen, E. I. Moses, A. Nikroo, R. Petrasso, T. C. Sangster, P. T. Springer, S. Batha, R. Benedetti, L. Bernstein, R. Betti, D. L. Bleuel, T. R. Boehly, D. K. Bradley, J. A. Caggiano, D. A. Callahan, P. M. Celliers, C. J. Cerjan, K. C. Chen, D. S. Clark, G. W. Collins, E. L. Dewald, L. Divol, S. Dixit, T. Doeppner, D. H. Edgell, J. E. Fair, M. Farrell, R. J. Fortner, J. Frenje, M. G. Gatu John-

- son, E. Giraldez, V. Y. Glebov, G. Grim, B. A. Hammel, A. V. Hamza, D. R. Harding, S. P. Hatchett, N. Hein, H. W. Herrmann, D. Hicks, D. E. Hinkel, M. Hoppe, W. W. Hsing, N. Izumi, B. Jacoby, O. S. Jones, D. Kalantar, R. Kauffman, J. L. Kline, J. P. Knauer, J. A. Koch, B. J. Koziolowski, G. Kyrala, K. N. LaFortune, S. L. Pape, R. J. Leeper, R. Lerche, T. Ma, B. J. MacGowan, A. J. MacKinnon, A. MacPhee, E. R. Mapoles, M. M. Marinak, M. Mauldin, P. W. McKenty, M. Meezan, P. A. Michel, J. Milovich, J. D. Moody, M. Moran, D. H. Munro, C. L. Olson, K. Opachich, A. E. Pak, T. Parham, H.-S. Park, J. E. Ralph, S. P. Regan, B. Remington, H. Rinderknecht, H. F. Robey, M. Rosen, S. Ross, J. D. Salmonson, J. Sater, D. H. Schneider, F. H. Sguin, S. M. Sepke, D. A. Shaughnessy, V. A. Smalyuk, B. K. Spears, C. Stoeckl, W. Stoeffl, L. Suter, C. A. Thomas, R. Tommasini, R. P. Town, S. V. Weber, P. J. Wegner, K. Widman, M. Wilke, D. C. Wilson, C. B. Yeamans, and A. Zylstra, *Physics of Plasmas* (1994-present) **20**, 070501 (2013).
- <sup>40</sup>J. Lindl, O. Landen, J. Edwards, E. Moses, and N. Team, *Physics of Plasmas* **21**, 020501 (2014), <http://dx.doi.org/10.1063/1.4865400>.
- <sup>41</sup>J. R. Rygg, J. A. Frenje, C. K. Li, F. H. Séguin, R. D. Petrasso, D. D. Meyerhofer, and C. Stoeckl, *Phys. Rev. E* **80**, 026403 (2009).
- <sup>42</sup>C. Cerjan, P. T. Springer, and S. M. Sepke, *Physics of Plasmas* **20**, 056319 (2013).
- <sup>43</sup>Springer, P.T., Cerjan, C., Betti, R., Caggiano, J.A., Edwards, M.J., Frenje, J.A., Glebov, V.Yu., Glenzer, S.H., Glenn, S.M., Izumi, N., Jones, O., Kyrala, G., Ma, T., McNaney, J., Moran, M., Munro, D.H., Regan, S., Sangster, T.C., Sepke, S., Scott, H., Town, R.P.J., Weber, S.V., and Wilson, B., *EPJ Web of Conferences* **59**, 04001 (2013).
- <sup>44</sup>H. G. Rinderknecht, M. G. Johnson, A. B. Zylstra, N. Sinenian, M. J. Rosenberg, J. A. Frenje, C. J. Waugh, C. K. Li, F. H. Sguin, R. D. Petrasso, J. R. Rygg, J. R. Kimbrough, A. MacPhee, G. W. Collins, D. Hicks, A. Mackinnon, P. Bell, R. Bionta, T. Clancy, R. Zacharias, T. Dppner, H. S. Park, S. LePape, O. Landen, N. Meezan, E. I. Moses, V. U. Glebov, C. Stoeckl, T. C. Sangster, R. Olson, J. Kline, and J. Kilkenny, *Review of Scientific Instruments* **83**, 10D902 (2012).
- <sup>45</sup>N. Sinenian, M. J.-E. Manuel, A. B. Zylstra, M. Rosenberg, C. J. Waugh, H. G. Rinderknecht, D. T. Casey, H. Sio, J. K. Ruszczyński, L. Zhou, M. G. Johnson, J. A. Frenje, F. H. Séguin, C. K. Li, R. D. Petrasso, C. L. Ruiz, and R. J. Leeper, *Review of Scientific Instruments* **83**, 043502 (2012).
- <sup>46</sup>J. Ziegler, J. Biersack, and U. Littmark, *The stopping and range of ions in matter* (Pergamon, New York, 1985).
- <sup>47</sup>T. Ma, P. K. Patel, N. Izumi, P. T. Springer, M. H. Key, L. J. Atherton, L. R. Benedetti, D. K. Bradley, D. A. Callahan, P. M. Celliers, C. J. Cerjan, D. S. Clark, E. L. Dewald, S. N. Dixit, T. Döppner, D. H. Edgell, R. Epstein, S. Glenn, G. Grim, S. W. Haan, B. A. Hammel, D. Hicks, W. W. Hsing, O. S. Jones, S. F. Khan, J. D. Kilkenny, J. L. Kline, G. A. Kyrala, O. L. Landen, S. Le Pape, B. J. MacGowan, A. J. Mackinnon, A. G. MacPhee, N. B. Meezan, J. D. Moody, A. Pak, T. Parham, H.-S. Park, J. E. Ralph, S. P. Regan, B. A. Remington, H. F. Robey, J. S. Ross, B. K. Spears, V. Smalyuk, L. J. Suter, R. Tommasini, R. P. Town, S. V. Weber, J. D. Lindl, M. J. Edwards, S. H. Glenzer, and E. I. Moses, *Phys. Rev. Lett.* **111**, 085004 (2013).